A two-phase model for compaction and damage 2. Applications to compaction, deformation and the role of interfacial surface tension

Yanick Ricard

Laboratoire de Sciences de la Terre, Ecole Normale Supérieure de Lyon, Lyon, France

David Bercovici[1]

Department of Geology and Geophysics, University of Hawai'i at Mānoa, Honolulu, Hawai'i

Gerald Schubert

Department of Earth and Space Sciences, University of California, Los Angeles, California

Abstract. New equations for the dynamics of a two-phase mixture are derived in a companion paper [*Bercovici et al.*, this issue (a)]. These equations do not invoke a bulk viscosity as most previous papers have done, and use the existence of the pressure difference between the two phases, including the possibility of surface energy at the interface between the phases. In this paper we show how a two-phase mixture reacts to simple stress fields. As a basic example, we discuss the deformation of a porous material confined by an impermeable jacket and loaded by a porous piston and show that the fluid can never be totally extracted from the matrix. We demonstrate that an unconfined porous sample is stronger under shear deformation than under normal stress. We consider spherically symmetric compaction and show that some unphysical results obtained using a constant matrix bulk viscosity are naturally avoided in our approach. We discuss the problem of compaction of a two-phase liquid in the presence of surface tension. In a one-dimensional simulation the surface tension generates porosity instabilities that tend to localize the fluid into narrow sills and dikes that cannot reach the surface.

1. Introduction

The equations of two-phase viscous flow have been initially developed in the geophysical community by *McKenzie* [1984, 1985, 1987], *Richter and McKenzie* [1984], and *Scott and Stevenson* [1984] (see also *Drew and Passman* [1999] for a review of the general theory of multicomponent fluids). Since then, they have been widely used [e.g., *Ribe*, 1985, 1987; *Fowler*, 1990a, 1990b; *Turcotte and Phipps Morgan*, 1992; *Spiegelman*, 1993a, 1993b, 1993c; *Schmeling*, 2000]. We have proposed a different set of mechanical equations for two-phase viscous flow in the companion paper [*Bercovici et al.*, this issue (a)] (herein after referred to as BRS1). Our equations have various differences with previous approaches, the most salient of which are that (1) they do not require the existence of a matrix bulk viscosity when the two phases are incompressible, (2) they account for surface energy at the interface between the phases, and (3) they assume that the two phases retain their own pressure fields. The mass and momentum conservation equations proposed

[1] Now at Department of Geology and Geophysics, Yale University, New Haven, Connecticut.

in BRS1 are

$$\frac{\partial \phi}{\partial t} + \boldsymbol{\nabla} \cdot [\phi \mathbf{v}_f] = 0, \tag{1}$$

$$\frac{\partial (1-\phi)}{\partial t} + \boldsymbol{\nabla} \cdot [(1-\phi) \mathbf{v}_m] = 0, \tag{2}$$

$$\begin{aligned} -\phi \left[\boldsymbol{\nabla} P_f + \rho_f g \hat{\mathbf{z}}\right] + \boldsymbol{\nabla} \cdot [\phi \underline{\boldsymbol{\tau}}_f] \\ + c \Delta \mathbf{v} + \phi \left[\Delta P \boldsymbol{\nabla} \phi + \boldsymbol{\nabla} (\sigma \alpha)\right] = 0, \end{aligned} \tag{3}$$

$$\begin{aligned} -(1-\phi) \left[\boldsymbol{\nabla} P_m + \rho_m g \hat{\mathbf{z}}\right] + \boldsymbol{\nabla} \cdot [(1-\phi) \underline{\boldsymbol{\tau}}_m] \\ - c \Delta \mathbf{v} + (1-\phi) \left[\Delta P \boldsymbol{\nabla} \phi + \boldsymbol{\nabla} (\sigma \alpha)\right] = 0. \end{aligned} \tag{4}$$

where $\Delta \mathbf{v} = \mathbf{v}_m - \mathbf{v}_f$ and $\Delta P = P_m - P_f$. The fluid and matrix phases, referred to by the indices f and m, have volume fractions ϕ and $1 - \phi$, respectively. Although these indices will correspond to the different phases, the equations have been written in a perfectly symmetric way and are invariant to a permutation of f and m and ϕ and $1 - \phi$; this symmetry property is referred to as material invariance (BRS1). The volume-averaged velocities of each phase are $\mathbf{v}_m$ and $\mathbf{v}_f$ and their pressures P_m and P_f (see BRS1).

Alternatively, instead of writing the equations of mass and momentum conservation of each phase, we can write mixture and difference equations. Defining the average and difference of any quantity q as $\bar{q} = \phi q_f + (1-\phi) q_m$ and $\Delta q = q_m - q_f$, respectively, one easily obtains by linear combination of (1)-(4) a new set of equivalent equations:

$$\boldsymbol{\nabla} \cdot \bar{\mathbf{v}} = 0, \tag{5}$$

$$\frac{\overline{D} \phi}{D t} = \boldsymbol{\nabla} \cdot [\phi (1-\phi) \Delta \mathbf{v}], \tag{6}$$

where $\bar{D}/Dt$ is defined by $\partial/\partial t + \bar{\mathbf{v}} \cdot \boldsymbol{\nabla}$,

$$-\boldsymbol{\nabla} \bar{P} + \boldsymbol{\nabla} \cdot \bar{\underline{\boldsymbol{\tau}}} - \bar{\rho} g \hat{\mathbf{z}} + \boldsymbol{\nabla} (\sigma \alpha) = 0, \tag{7}$$

$$\begin{aligned} -\phi (1-\phi) \left[\boldsymbol{\nabla} \Delta P + \Delta \rho g \hat{\mathbf{z}}\right] \\ + \boldsymbol{\nabla} \cdot [\phi (1-\phi) \Delta \underline{\boldsymbol{\tau}}] - \bar{\underline{\boldsymbol{\tau}}} \cdot \boldsymbol{\nabla} \phi - c \Delta \mathbf{v} = 0. \end{aligned} \tag{8}$$

These equations express the total mass conservation, the porosity transport, the total momentum equilibrium and the action-reaction principle.

In (4), (7), and (8) the stress tensor for the phase m is defined by

$$\underline{\boldsymbol{\tau}}_m = \mu_m \left(\boldsymbol{\nabla} \mathbf{v}_m + [\boldsymbol{\nabla} \mathbf{v}_m]^t - \frac{2}{3} \boldsymbol{\nabla} \cdot \mathbf{v}_m \underline{\mathbf{I}} \right), \tag{9}$$

and a symmetric expression holds for the f phase, with f replacing m. The viscosities μ_m and μ_f are the constant viscosities of each individual phase. BRS1 have advocated that

the mixture of two incompressible fluids cannot be materially invariant and have a bulk viscosity; thus bulk viscosity is not used, in contrast to the approach of previous papers [*McKenzie*, 1984; *Spieglman*, 1993a, 1993b, 1993c; *Schmeling*, 2000] where an extra term, $\zeta \boldsymbol{\nabla} \cdot \mathbf{v}_m \underline{\mathbf{I}}$, is present on the right side of (9) (see Appendix A for a more detailed comparison of our equations with those of *McKenzie* [1984]).

The interaction coefficient c can be chosen in such a way that it retains the symmetry of the momentum equations while still leading to the usual Darcy term when $\mu_f \ll \mu_m$:

$$c = \frac{\mu_m \mu_f \phi^2 (1-\phi)^2}{\mu_f k(1-\phi)\phi^2 + \mu_m k(\phi)(1-\phi)^2} \tag{10}$$

(see BRS1), where the permeability $k(\phi)$ is a function of porosity ϕ. Usually, $k(\phi)$ is taken to vary like $k_0 \phi^n$, where n is ∼2-3. The parameter k_0 has the dimensions of area and is physically related to the cross-sectional area of the pores ($k_0 \sim 10^{-9} - 10^{-10}$ m^2). In the following, we adopt the common and simplifying assumption that $n = 2$, which implies that c is a constant

$$c = \frac{\mu_m \mu_f}{k_0(\mu_m + \mu_f)}, \tag{11}$$

and when $\mu_f \ll \mu_m$, $c \sim \mu_f / k_0$.

Our model takes into account the surface tension σ at the interface between the two phases. The interface density α, i.e., the area of interface per unit volume, is a function of porosity and vanishes when the mixture becomes a single-phase medium, i.e., when $\phi = 0$ or $\phi = 1$. We generalize a suggestion by *Ni and Beckermann* [1991] and assume

$$\alpha = \alpha_0 \phi^a (1-\phi)^b, \tag{12}$$

where the exponents a and b are between 0 and 1. This expression is in agreement with that obtained for a hexagonal net of matrix grains when $a = b = 1/2$ [*Stevenson*, 1986; *Riley et al.*, 1990, *Riley and Kohlstedt*, 1991]. If $1/\langle R \rangle$ is the average interface curvature (defined to be positive when the interface is concave to the fluid phase and negative when convex to the fluid), then it can be shown (see BRS1) that

$$\frac{2}{\langle R \rangle} = \frac{d\alpha}{d\phi} = \alpha_0 \frac{a - \phi(a+b)}{\phi^{(1-a)}(1-\phi)^{(1-b)}}. \tag{13}$$

One important physical implication of (13) is that the stress induced by surface tension $\sigma(d\alpha/d\phi)$ will become potentially infinite when ϕ goes to 0 or 1. Moreover, the interface curvature changes sign when $\phi = \phi_c = a/(a+b)$; this effect is associated with a change of dihedral angle from $\geq 60^o$ to $\leq 60^o$ [see *McKenzie*, 1984; *Kohlstedt*, 1992] (although, in fact, two-phase theory does not account for grain-grain interfaces relative to which the dihedral angle is measured). A very small ϕ_c thus correlates with the fluid phase or melt becoming interconnected at low porosities.

The set (1)-(4) is still not complete. It is easy to realize that one more equation is needed, for example, an equation

relating P_m and P_f. We know that in the case of adiabatic equilibrium with no motion and a constant surface tension, the Laplace condition should apply:

$$\Delta P + \sigma \frac{d\alpha}{d\phi} = 0. \tag{14}$$

However BRS1 have shown that this often used condition [e.g., *Drew*, 1983; *Ni and Beckerman* 1991], may not generally hold. When motion occurs, the surface tension should no longer equilibrate the pressure discontinuity but rather the normal stress discontinuity [*Landau and Lifshitz*, 1959]. In the case of variable surface tension, i.e., a temperature-dependent σ, a discontinuity in shear stress should also occur across interfaces. This is often called the Marangoni effect [*Landau and Lifshitz*, 1959]. There is also no reason for processes occurring at the interface between the two phases to be adiabatic.

Accordingly, BRS1 have proposed a more general, albeit more complex, condition which yields

$$\Delta P \frac{\overline{D}\phi}{Dt} + \sigma \frac{\overline{D}\alpha}{Dt} = -K_0 \frac{(\mu_m + \mu_f)}{\phi(1-\phi)} \left(\frac{\overline{D}\phi}{Dt} \right)^2 + f\Psi, \tag{15}$$

where K_0 is a constant related to the topology of the interface and Ψ is the deformational work

$$\Psi = c\Delta v^2 + \phi \boldsymbol{\nabla} \mathbf{v}_f : \underline{\boldsymbol{\tau}}_f + (1-\phi) \boldsymbol{\nabla} \mathbf{v}_m : \underline{\boldsymbol{\tau}}_m. \tag{16}$$

As shown by BRS1, K_0 is of order 1. In (15), f is interpreted as a partitioning coefficient (from 0 to 1) that characterizes the percentage of deformational work that, rather than being dissipated as viscous heating, acts to deform the interface and is thus effectively conservative, or reversible, since it is stored as interfacial surface energy. The existence of both stored and dissipative components of the deformational work in media with internal microstructure, such as defects, has been recognized since at least the 1930s [*Farren and Taylor*, 1925; *Taylor and Quinney*, 1934].

When the characteristic velocity of an experiment is divided by X, the rate of porosity change is also decreased by the same coefficient, whereas the terms on the right-hand side of (15) are decreased by X^2. Therefore the Laplace condition (14) appears, as it should, from (15) when the deformation rates go to zero. However, in all situations where the porosity evolves with time, the matrix and the fluid pressures cannot be assumed equal contrary to what was assumed in some previous papers (see Appendix A) [*McKenzie*, 1984; *Spiegelman*, 1993a, 1993b, 1993c; *Schmeling*, 2000].

In this paper we will assume that the partitioning coefficient f is zero. In a companion paper by *Bercovici et al.*, [this issue (b)] we will show that in cases far from equilibrium, i.e., when $f \neq 0$, our equations provide a damage theory which predicts shear localization. Surface tension σ will also be taken as a constant. These assumptions significantly simplify the two Navier-Stokes equations (3) and (4)

and imply that the pressure jump condition is

$$\Delta P + \sigma \frac{d\alpha}{d\phi} = -K_0 \frac{(\mu_m + \mu_f)}{\phi(1-\phi)} \boldsymbol{\nabla} \cdot [\phi(1-\phi)(\mathbf{v}_m - \mathbf{v}_f)]. \quad (17)$$

In the following sections we will examine a series of problems, beginning with the simplest idealized cases of forced compaction and deformation, without surface tension, to illustrate the most basic applications; these will include one-dimensional compaction and shear, two-dimensional uniaxial compression, and three-dimensional spherical compaction. We will then close by examining gravitationally forced compaction with and without interfacial surface tension for simple applications to magma percolation problems. We will compare our results when appropriate with those obtained for the same examples but with different equations by *McKenzie* [1984] and *Richter and McKenzie* [1984]. We will use M84 and BRS to refer to the previously used set of equations (see Appendix A) and to our set of equations, respectively. M84 replaces the pressure jump condition (15) by $\Delta P = 0$ and introduces a bulk viscosity in the rheological equation (9). In these comparisons we will assume that there is no surface tension and that $\mu_f \ll \mu_m$.

2. Behavior of a Mixture Under Simple Stress Fields

In this section we consider various examples of simple compaction and deformation. As a simplification, we assume no buoyancy effects, i.e., either gravity $g = 0$ or the matrix and fluid phases have the same densities ($\rho_m = \rho_f$). We also assume there is no surface tension on the interface between the phases ($\sigma = 0$). The fluid has a very small viscosity compared to that of the solid $\mu_f << \mu_m$ so we neglect the fluid viscous stresses $\underline{\tau}_f$.

2.1. One-Dimensional Forced Compaction

We first consider a layer of thickness l_0, infinite in horizontal extent and containing a mixture of uniform porosity ϕ_0. The system is assumed to be one-dimensional such that $\mathbf{v}_m = v_{m_z}(z,t)\hat{\mathbf{z}}$, $\mathbf{v}_f = v_{f_z}(z,t)\hat{\mathbf{z}}$ and $\phi = \phi(z,t)$, and the bottom boundary of the layer, at $z = 0$, is impermeable ($v_{f_z} = v_{m_z} = 0$ at $z = 0$).

In this example, the mixture conservation equation (5) can be integrated taking into account the boundary condition at $z = 0$ yielding

$$\phi v_{f_z} + (1-\phi) v_{m_z} = 0. \quad (18)$$

This shows that the matrix and fluid velocities must have opposite signs and that the only way to compact the matrix is to allow the fluid to be expelled through a porous piston. This experiment corresponds to what happens in some coffee filters or coffee presses, where a thin metallic screen pushed

through a coffee-water mixture separates the coffee from the grounds (see Figure 1).

We consider that the top of the matrix is pushed down at constant velocity $-v_0$ and that the position of the piston at time t is $l_0 - v_0 t$. Obviously, the maximum time of the experiment has to be shorter than $\tau = l_0\phi_0/v_0$, the time at which all the fluid will be extracted and where only matrix grains will remain below the piston.

The problem can be solved in terms of v_{m_z} and ϕ only by combining the action-reaction equation (8) with (17) and (18). With the assumption $\sigma = 0$, we obtain

$$\delta_m^2\phi^2\Big(\kappa(1-\phi)\frac{\partial}{\partial z}\left[\frac{1}{\phi(1-\phi)}\frac{\partial(1-\phi)v_{m_z}}{\partial z}\right] + \frac{\partial}{\partial z}\left[(1-\phi)\frac{\partial v_{m_z}}{\partial z}\right]\Big) - v_{m_z} = 0, \quad (19)$$

where $\kappa = 3K_0/4$, and then the porosity can be updated using (2). Equation (19) displays a basic length scale, i.e., the compaction length

$$\delta_m \equiv \sqrt{\frac{4\mu_m}{3c}} \quad (20)$$

(for simplicity, here and in the following, we assume that c is a constant). Our definition of the compaction length δ_m is different from those of both *McKenzie* [1984], who uses $\phi_0\sqrt{(\zeta + 4\mu_m/3)/c}$, and *Stevenson* [1986], who uses $\sqrt{\mu_m/c}$. In the case of constant porosity $\phi = \phi_0$, it is useful to define another length scale by

$$h = \delta_m\sqrt{\phi_0(1-\phi_0)(\kappa+\phi_0)}. \quad (21)$$

When the porosity is small, $\phi_0 << \kappa \sim 0.75$, the compaction is controlled by the difference in pressures between the two phases rather than by the normal stress in the matrix.

For geophysical applications on melt extraction, $k_0 \sim 5 \times 10^{-10}$ m^2, $\mu_m \sim 10^{18}$ Pa s, and the magma viscosity can vary from $\mu_f \sim 10$ Pa s (oceanic spreading ridge basalt) to $\mu_f \sim 10^4$ Pa s (wet siliceous melt) and to $\mu_f \sim 10^{10}$ Pa s (dry siliceous melt). These three magmas correspond to compaction lengths of 8 km, 250 m, and 30 cm, respectively.

An analytical solution to (19) is easily derived in the case of a spatially constant porosity $\phi = \phi_0$ (i.e., we can only derive the exact solution at $t = 0$ but not at further times when porosity has evolved). The integration constants are obtained from the values of the matrix velocity on the top $v_{m_z}(l_0) = -v_0$ and at the bottom $v_{m_z}(0) = 0$. The fluid pressure is also set to zero at the top. After some algebra we obtain

$$v_{f_z}(z) = v_0\frac{(1-\phi_0)}{\phi_0}\frac{\sinh(z/h)}{\sinh(l_0/h)}, \quad (22)$$

$$v_{m_z}(z) = -v_0\frac{\sinh(z/h)}{\sinh(l_0/h)}, \quad (23)$$

$$P_f(z) = \frac{4\mu_m v_0}{3}\frac{h}{\delta_m^2\phi_0^2}\frac{[\cosh(l_0/h) - \cosh(z/h)]}{\sinh(l_0/h)}, \quad (24)$$

$$P_m(z) = \frac{4\mu_m v_0}{3}\frac{h}{\delta_m^2\phi_0^2}\frac{1}{\sinh(l_0/h)} \cdot \left[\cosh(l_0/h) - \cosh(z/h)\left(1 - \kappa\phi_0\frac{\delta_m^2}{h^2}\right)\right], \quad (25)$$

$$\tau_{m_{zz}}(z) = -\frac{4\mu_m v_0}{3h}\frac{\cosh(z/h)}{\sinh(l_0/h)}. \quad (26)$$

From these expressions we see that the force per unit surface across the mixture, $\Sigma = \phi_0(-P_f + \tau_{f_{zz}}) + (1 - \phi_0)(-P_m + \tau_{m_{zz}})$, is independent of depth and corresponds to the force per area exerted on the piston; i.e.,

$$\Sigma = -\frac{4\mu_m v_0}{3}\frac{h}{\delta_m^2\phi_0^2}\frac{1}{\tanh(l_0/h)} \quad (27)$$

(by sign convention for Σ, opposite to that of pressure, the fluid is expelled when Σ is negative). The fact that Σ is a constant is an obvious requirement of the mechanical equilibrium of the fluid and could have been deduced from the Navier-Stokes equation of the mixture (7).

From the experimenter's point of view the system behaves like a dashpot with a friction coefficient ν,

$$\nu = -\frac{l_0\Sigma}{v_0} = \frac{4\mu_m}{3}\left(\frac{h}{\delta_m\phi_0}\right)^2\frac{l_0/h}{\tanh(l_0/h)}. \quad (28)$$

The normalized coefficient ν/μ_m is depicted in Figure 2 as a function of ϕ_0 for 2 values of l_0/δ_m (we arbitrarily choose $l_0/\delta_m = 0.1,\ 10$). When the porosity goes to zero, ν goes to infinity and the mixture becomes a single phase incompressible matrix. As $\phi_0 \to 1$, the friction coefficient approaches 0, and the fluid can escape freely through the piston (strictly speaking, neglecting $\phi_0\underline{\boldsymbol{\tau}}_f$ with respect to $(1 - \phi_0)\underline{\boldsymbol{\tau}}_m$ becomes impossible when $\phi_0 = 1$). An increased l_0 at constant porosity and compaction length increases the friction coefficient: the energy cost to drive the Darcy flow becomes large and the matrix appears stiffer. The minimum friction coefficient is obtained in the limit $l_0/h \to 0$ (negligible Darcy term) in which case

Figure 2

$$\min(\nu) \sim \frac{4\mu_m}{3}(1 - \phi_0)\left(1 + \frac{\kappa}{\phi_0}\right), \quad (29)$$

The same coffee-press example can readily be done with the M84 equations that contain an intrinsic bulk viscosity in the rheological equation and assume the equality of pressures (see Appendix A). The analytical solution (28) for $\phi = \phi_0$ becomes

$$\nu_\zeta = \frac{(4\mu_m + 3\zeta)}{3}(1 - \phi_0)\frac{l_0/h_\zeta}{\tanh(l_0/h_\zeta)}, \quad (30)$$

where h_ζ is defined by

$$h_\zeta^2 \equiv \frac{(4\mu_m + 3\zeta)}{3c}\phi_0^2(1-\phi_0). \tag{31}$$

In this case, when the Darcy term is negligible $l_0/h << 1$,

$$\min(\nu_\zeta) = \frac{(4\mu_m + 3\zeta)}{3}(1-\phi_0). \tag{32}$$

Since bulk viscosity has never been measured, most authors have assumed $\zeta = \mu_m$. However, the comparison of (29) with (32) and Appendix A show that a ζ of order μ_m/ϕ_0 would have been more appropriate (of course, when the porosity is not uniform, a comparison of the two theories is more difficult). According to our equations the fluid is more difficult to extract under one-dimensional forced compaction than previously estimated. A similar conclusion has been obtained by *Schmeling* [2000] using a different approach based on averaging methods for an elastic medium containing heterogeneities [*O'Connell and Budiansky*, 1977; *Schmeling*, 1985].

The analytic expression for the change in porosity at time $t = 0$,

$$\frac{\partial\phi}{\partial t} = -(1-\phi_0)\frac{v_0}{h}\frac{\cosh(z/h)}{\sinh(l_0/h)}, \tag{33}$$

suggests the formation of a compacted boundary layer. The porosity decreases mostly near the top, and this tends to close the pathways needed by the fluid to percolate through the matrix. To understand what happens in later stages of the experiment, i.e., when the porosity is no longer constant in depth, we must solve the equations numerically. We solve (19) with a finite difference tridiagonal solver after a change of variable to work on a regular grid, then update the porosity explicitly using (2).

Figure 3 depicts the variation with depth of the porosity (Figure 3a) and velocity (Figure 3b) at various times. The depth is normalized by l_0. The piston, which is at $z/l_0 = 1$ at the beginning, is moved down to $z/l_0 = 0.95$ at the end. Not all the fluid can be expelled from the mixture. In particular, the experiment ends when the porosity near the piston reaches 0, therefore sealing the layer. With the chosen numerical values this happens at $t/\tau = 0.83$, which means that 17% of the fluid remains trapped in the matrix below the compacted boundary layer.

Figure 3

The velocity profiles depicted in Figure 3b show that until the surface porosity reaches 0, the velocity profiles are quite linear. The decrease in the porosity near the piston arises from an effective compaction that is induced by the matrix material collecting against the piston during its downward motion. In fact, it is easily verified in the coffee-press experiment (Figure 1) that as the piston is pushed down through a well stirred mixture of water and coffee grounds, the grounds accumulate on top and indeed plug the filter. As a consequence, to maintain a significant velocity, a larger pressure must be applied.

The force per unit surface that has be be exerted on top of the mixture, $\Sigma(t)$ varies through time. It is transmitted through the mixture as pressure and viscous stress. Assuming that the expelled fluid is removed so that P_f remains zero near the piston, the system is equivalent to a dashpot with a time-dependent friction coefficient

$$\nu(t) = \frac{l_0}{v_0}\left[(1-\phi)\left(\frac{4\mu_m}{3}\frac{\partial v_{m_z}}{\partial z} - P_m\right)\right]_{z=l_0-v_0 t}. \quad (34)$$

When $t = 0$, this friction coefficient must be equal to that predicted by (28) ($\nu/\mu_m \sim 24$ when $(l_0/(\delta_m\phi_0))^2 = 0.1$ and $\phi_0 = 0.05$).

The evolution of $\nu(t)/\mu_m$ is shown in Figure 4 as a function of t/τ. The force per unit surface that must be exerted to push the piston at constant velocity is proportional to this normalized friction coefficient, and $\nu(t=0)$ is exactly that predicted by the analytical expression (28) (horizontal dashed line). As fluid is expelled, the porosity decreases and a larger force has to be exerted until a singularity occurs near $t/\tau = 0.83$, where $\phi(1)$ reaches 0.

Figure 4

2.2. Deformation Under Shear

The friction coefficient ν that has been obtained from (28) is possibly larger than the matrix viscosity μ_m. However, this effect reflects the fact that ν includes resistance to compression of matrix grains, which approaches infinity as ϕ goes to zero. Thus ν is not truly analogous to viscosity. Indeed, on a macroscopic average, the mixture viscosity is smaller than that of a pure matrix.

Let us again consider a layer infinite in the x and y directions but with thickness $2l_0$ (such that $-l_0 \le z \le +l_0$) and in which porosity is constant and equal to ϕ_0. A standard experimental approach to measuring macroscopic viscosity is to submit this layer to simple shear by imposing horizontal velocities $v_{m_x} = v_{f_x} = \pm v_0$ at $z = \pm l_0$. The obvious solution of (1)-(4) and (17) (with σ and $\Delta\rho g = 0$) is simply

$$v_{m_x} = v_{f_x} = v_0\frac{z}{l_0}, \quad (35)$$

$$v_{fz} = v_{mz} = 0. \quad (36)$$

In order to impose this deformation, a shear stress $(1-\phi_0)\tau_{m_{xz}} = (1-\phi_0)\mu_m(v_0/l_0)$ must be applied. This shows that under shear the mixture behaves like a homogeneous Newtonian body with viscosity $(1-\phi_0)\mu_m$. The same result would also have been obtained using M84 as the deformation occurs without dilation of the matrix.

2.3. Two-Dimensional Uniaxial Compression

Another way to measure equivalent viscosity is to subject a sample to uniaxial compression. We consider a sample with square cross section in the x-z plane (where $|x| \le l_0$, $|z| \le l_0$) but infinite in y; the sample is squeezed in the z direction by impermeable pistons with imposed vertical

velocities, $-v_0$ on the top ($z = +l_0$) and v_0 at the bottom ($z = -l_0$). We assume that the matrix and fluid have the same vertical velocities

$$v_{m_z} = v_{f_z} = -v_0 \frac{z}{l_0}; \tag{37}$$

we can verify that these expressions are exact solutions when the contacts between the pistons and the sample correspond to free slip conditions. The square section is unconstrained laterally (in the x direction), and the fluid and matrix have different horizontal velocities v_{f_x} and v_{m_x}. As in section 2.2 we search for solutions with $\sigma = 0$ and $\Delta\rho g = 0$ and with a constant initial porosity ϕ_0, i.e., solutions are only valid near $t = 0$.

With the above assumptions, the total mass conservation (5) can be integrated in x and yields

$$\phi_0 v_{f_x} + (1-\phi_0) v_{m_x} = v_0 \frac{x}{l_0}, \tag{38}$$

while the action-reaction equation (8) results in

$$\frac{h^2}{\phi_0} \frac{\partial^2 v_{m_x}}{\partial x^2} - (v_{m_x} - v_{f_x}) = 0, \tag{39}$$

where h is the length parameter defined in (21). Then the fluid pressure P_f can be deduced from the fluid momentum equation (3), and the matrix pressure P_m can be deduced from the pressure condition (17).

We solve these equations with the boundary conditions that both the fluid pressure and the horizontal normal component of the matrix total stress, $-P_m + 2\mu_m(\partial v_{m_x}/\partial x - (1/3)\boldsymbol{\nabla}\cdot\mathbf{v}_m)$, vanish at $x = \pm l_0$. After some algebra we obtain

$$v_{f_x} = v_0 \frac{x}{l_0} + v_0 \frac{3h}{2l_0} \frac{(1-\phi_0)}{(\kappa+\phi_0)} \frac{\sinh(x/h)}{\cosh(l_0/h)}, \tag{40}$$

$$v_{m_x} = v_0 \frac{x}{l_0} - v_0 \frac{3h}{2l_0} \frac{\phi_0}{(\kappa+\phi_0)} \frac{\sinh(x/h)}{\cosh(l_0/h)}, \tag{41}$$

$$P_f = 2(1-\phi_0) \frac{\mu_m v_0}{l_0} \left(1 - \frac{\cosh(x/h)}{\cosh(l_0/h)}\right), \tag{42}$$

$$P_m = 2(1-\phi_0) \frac{\mu_m v_0}{l_0} \cdot \left[1 - \left(1 - \kappa\phi_0 \frac{\delta_m^2}{h^2}\right) \frac{\cosh(x/h)}{\cosh(l_0/h)}\right], \tag{43}$$

$$\begin{aligned} \Sigma &= (1-\phi_0)\tau_{m_{zz}} - \phi_0 P_f - (1-\phi_0) P_m \\ &= -4(1-\phi_0) \frac{\mu_m v_0}{l_0} \left(1 - \frac{\phi_0}{(\kappa+\phi_0)} \frac{\cosh(x/h)}{\cosh(l_0/h)}\right), \end{aligned} \tag{44}$$

The quantity Σ in (44) is the force per unit surface that has to be exerted by the experimenter on both pistons. When a

similar experiment is performed with a homogeneous Newtonian viscous fluid, the ratio between the applied pressure and the shortening rate is simply -4 times the viscosity. The equivalent viscosity η of the mixture under uniaxial compression is therefore $-l_0\langle\Sigma\rangle/(4v_0)$, where $\langle\Sigma\rangle$ is the x-averaged Σ. This leads to the apparent viscosity

$$\eta = \mu_m(1-\phi_0)\left[1 - \frac{h}{l_0}\frac{\phi_0}{(\kappa+\phi_0)}\tanh(l_0/h)\right], \quad (45)$$

which is always smaller than μ_m and slightly smaller than the shear mixture viscosity $(1-\phi_0)\mu_m$. It is, however, always larger than $(1/4)\mu_m\kappa(1-\phi_0)/(\kappa+\phi_0)$, which is obtained when $l_0/\delta_m \sim 0$.

Figure 5 depicts the equivalent viscosity of the mixture according to (45) (solid lines labelled BRS). When $\phi_0 = 1$, the equivalent viscosity tends to the fluid viscosity which is zero in our approximation. As soon as $\phi_0 > l_0/\delta_m$, the equivalent viscosity decreases. A large sample always looks stiffer than a smaller one because Darcy flow can draw and expel fluid from essentially everywhere in a small sample but can only draw fluid from proximal regions in a large sample, and thus not all fluid is readily squeezed from a large sample. When l_0/δ_m is large, the viscosities measured under shear or normal stresses are equal.

Figure 5

If we were to use M84 equations, instead of (45) we would obtain

$$\eta_\zeta = (1-\phi_0)\mu_m\left[1 - \frac{h_\zeta}{l_0}\frac{3\mu_m}{(4\mu_m+3\zeta)}\tanh\left(\frac{l_0}{h_\zeta}\right)\right], \quad (46)$$

where h_ζ has been defined by (31). Although both theories, with and without bulk viscosities, predict the same behavior at $\phi_0 = 0$ or 1, BRS predicts that the mixture is significantly stiffer than when using M84, unless a bulk viscosity significantly larger than μ_m is chosen.

Squeezing of the mixture leads to expulsion of fluid as seen in Figure 6 where the matrix (Figure 6, bottom), and the fluid (Figure 6, top) velocities at $x = l_0$ are shown as functions of ϕ. When the porosity tends to 0 or 1, both the matrix and fluid velocities are v_0; that is the minor phase is simply advected by the major one (thick lines BRS). This is in contrast to the solutions obtained with the M84 set of equations, which lead to

Figure 6

$$v_{f_x} = v_0\frac{x}{l_0} + v_0\frac{h_\zeta}{l_0}\frac{(1-\phi_0)}{\phi_0}\frac{6\mu_m}{(4\mu_m+3\zeta)}\frac{\sinh(x/h_\zeta)}{\cosh(l_0/h_\zeta)} \quad (47)$$

$$v_{m_x} = v_0\frac{x}{l_0} - v_0\frac{h_\zeta}{l_0}\frac{6\mu_m}{(4\mu_m+3\zeta)}\frac{\sinh(x/h_\zeta)}{\cosh(l_0/h_\zeta)}. \quad (48)$$

With $\zeta = \mu_m$ and the porosity tending to zero, the fluid velocity at $x = l_0$ tends to a finite value equal to $(1+30/\sqrt{7})v_0$ (see Figure 6 dashed lines labeled M84). A very surprising prediction of (48) is that the horizontal extension of the overall mixture can correspond to horizontal compaction of the matrix phase. This happens for small samples, $l_0 << \delta_m$

such that Darcy flow draws fluid easily from most of the volume and for a bulk viscosity smaller than μ_m. In this case, the expulsion of fluid with so little Darcy resistance appears to be so fast that the matrix has to collapse in x to compensate for the excess loss of fluid. However, compaction of the matrix under extensive stresses does not occur with BRS unless $K_0 < \phi_0/2$, a condition in contradiction with the fact that K_0 is of order 1.

2.4. Radial Compaction

McKenzie [1984] proposed a method to measure experimentally the bulk viscosity (at least as a thought experiment) which entails squeezing a spherical two-phase body. We reexamine this thought experiment using both M84 and BRS. We again assume no surface tension, and thus the only difference between our equations and those of *McKenzie* [1984] is the use of a bulk viscosity ζ by M84 and the pressure jump condition (17) by BRS.

With zero buoyancy forces (g or $\Delta\rho = 0$) and zero surface tension ($\sigma = 0$) and the assumption that the fluid stress $\underline{\boldsymbol{\tau}}_f$ is negligible, the action-reaction equation (8) leads to

$$-\phi(1-\phi)\boldsymbol{\nabla}\Delta P + \phi\boldsymbol{\nabla}\cdot[(1-\phi)\underline{\boldsymbol{\tau}}_m] - c\Delta\mathbf{v} = 0. \quad (49)$$

The fluid and matrix velocities are related through the total mixture conservation (5). Adoption of spherical symmetry (wherein $\mathbf{v}_f = \hat{\mathbf{r}}v_{f_r}(r)$, $\mathbf{v}_m = \hat{\mathbf{r}}v_{m_r}(r)$, and r is the radius from the center of the sphere) results in $\phi v_{f_r} + (1-\phi)v_{m_r} = B/r^2$, where B is a constant; the solution is nonsingular at the origin only if $B = 0$ in which case

$$\phi v_{f_r} + (1-\phi)v_{m_r} = 0. \quad (50)$$

2.4.1. Sintering and hot-isostatic-pressing approximation. In what *McKenzie* [1984] refers to as the "sintering and hot isostatic pressing" approximation, the interaction force $c\Delta\mathbf{v}$ is neglected. Although we also neglect this term, for the moment, we must note that as is evident from (49), this approximation is only valid as long as ϕ is nonzero.

In our model, even with the sintering approximation, the fluid and matrix pressures cannot be equal. The requirement that the microscopic stresses normal to the complex interfaces match imposes an average pressure jump related to the rate of phase separation (see BRS1). In the case where the porosity is constant, according to (17) with $\mu_f << \mu_m$ and using (50),

$$\Delta P = -\frac{K_0\mu_m}{\phi_0}\frac{1}{r^2}\frac{\partial r^2 v_{m_r}}{\partial r}. \quad (51)$$

This expression can be introduced in the momentum equation (49) for which the only solution that is nonsingular at the origin is $v_{m_r} = Cr$, where C is a constant. This velocity yields a zero stress tensor and particularly a zero radial viscous stress $\tau_{m_{rr}} = 0$ regardless of C (because of the absence of bulk viscosity in BRS). Therefore only pressures are applied to the two phases in a pure isotropic compaction with constant porosity.

The experimenter that squeezes the sphere of mixture imposes a force per unit area on the fluid and matrix of

$$\Sigma_f = -P_f \tag{52}$$

$$\Sigma_m = \tau_{m_{rr}} - P_m = -P_m, \tag{53}$$

respectively. These two forces are applied in proportions ϕ_0 and $1-\phi_0$, respectively. When the two forces are equal (e.g., in an experiment where the surface is enclosed in a rubber membrane), P_m and P_f are equal, and therefore the pressure jump condition (51) implies that $v_{m_r} = 0$.

In the case where the sphere is enclosed by a porous membrane that allows the fluid to escape freely, $\Sigma_f = P_f = 0$ (in the sintering approximation, the fluid pressure is uniform and remains zero inside the matrix). The experimenter applies a force per unit area at the surface of the sphere of radius R, $\Sigma = (1-\phi_0)\Sigma_m(R)$, and (51) implies

$$\Sigma = 3K_0\mu_m \frac{(1-\phi_0)}{\phi_0}\frac{v_{m_r}}{R}. \tag{54}$$

Using the mass conservation relation

$$\frac{\partial \phi_0}{\partial t} = (1-\phi_0)\boldsymbol{\nabla}\cdot\mathbf{v}_m = 3(1-\phi_0)C, \tag{55}$$

we deduce that the porosity evolves at constant surface stress as

$$\frac{\partial \phi_0}{\partial t} = \phi_0 \frac{\Sigma}{\mu_m K_0}. \tag{56}$$

BRS predicts that at constant applied stress, the compaction velocity tends to zero when the porosity vanishes (54). In other words, the porosity does not evolve anymore, and thus cannot become negative, when it reaches zero (56).

The same thought experiment using M84 would have given [see *McKenzie*, 1984]

$$\Sigma = 3(1-\phi_0)\zeta\frac{v_{m_r}}{R} \tag{57}$$

$$\frac{\partial \phi_0}{\partial t} = \frac{\Sigma}{\zeta}. \tag{58}$$

Contrary to (56), (58) obtained using M84 with a constant bulk viscosity can allow negative porosities as the compaction velocity does not reach zero when $\phi_0 = 0$.

Figure 7 depicts the normalized ratio of the applied force to the radial strain rate $(\Sigma R)/(\mu_m v_{m_r})$ according to (57) and (54) (assuming $\zeta = \mu_m$ and $K_0 = 1$). We predict that it is much more difficult to extract the fluid than previously thought.

Figure 7

The previous solutions are obtained under the sintering approximation $c = 0$. In fact, with minor modifications the solutions also hold when the fluid phase is simply void (of course, replacing the fluid phase by void implies that the equations of mass and momentum conservations for the fluid

are meaningless). However, as already mentioned, as soon as the fluid phase is not void and has a nonzero viscosity, the Darcy term varies like $c\mathbf{v}_m/\phi$; thus its importance increases at vanishing porosity, and the term is no longer negligible. We only discuss the influence of this term using BRS equations, but a similar exercise can be done with M84 equations.

2.4.2. Beyond the sintering approximation. When keeping the Darcy term, the radial compaction of a spherical body satisfies (49) in spherical polar coordinates. If the nonradial components of $\mathbf{v}_m$ are zero, v_{m_r} satisfies

$$h^2 \frac{\partial}{\partial r}\left(\frac{1}{r^2}\frac{\partial r^2 v_{m_r}}{\partial r}\right) - v_{m_r} = 0, \tag{59}$$

where h has been defined in (21). The only solution to (59) which is nonsingular at the origin is

$$v_{m_r} = C\frac{h^2}{r^2}(r\cosh(r/h) - h\sinh(r/h)), \tag{60}$$

where C is an integration constant. Knowing v_{m_r}, the radial viscous stress is readily deduced

$$\tau_{m_{rr}} = \frac{4}{3}\mu_m C\frac{h}{r} \cdot \left[\left(3\frac{h^2}{r^2}+1\right)\sinh(r/h) - 3\frac{h}{r}\cosh(r/h)\right]. \tag{61}$$

Contrary to what happens with the sintering approximation, the stress tensor is no longer isotropic, $\tau_{m_{rr}} \neq \tau_{m_{\theta\theta}} = \tau_{m_{\psi\psi}}$. The Darcy force introduces a directional term that always breaks isotropy.

The fluid pressure is obtained by integration of the fluid momentum equation and the matrix pressure is then deduced from the pressure jump (51),

$$P_m = P_f - \frac{\mu_m}{\phi_0}K_0 C\frac{\sinh(r/h)}{r/h}. \tag{62}$$

In the case where the sphere is enclosed by a rubber membrane, mass continuity (50) implies, as in section 2.4.1, that $C = 0$ and that only the internal pressures P_m and P_f are equal and resist the force applied by the experimenter Σ. When the surrounding jacket is permeable, the pressure P_f is zero at the surface of the mixture and the resistance to deformation is due to both pressure and normal stress (which unlike in section 2.4.1 is nonzero). From $\Sigma = (1-\phi_0)(\tau_{m_{rr}} - P_m)$, where $\tau_{m_{rr}}$ and P_m are given by (61) and (62), one gets at $r = R$,

$$\Sigma = \frac{1}{3}\mu_m(1-\phi_0)\frac{v_{m_r}}{R} \cdot \frac{(12(h/R)+4+3K_0/\phi_0)\tanh(R/h) - 12h/R}{h/R - (h/R)^2\tanh(R/h)}, \tag{63}$$

which is in agreement with (54) when the compaction length, δ_m, goes to infinity. Figure 7 depicts the normalized overall resistance of the sphere as a function of ϕ_0. Here again, the mixture resistance is much larger than would have been estimated with M84 assuming a constant bulk viscosity in (57).

3. Melt Migration

3.1. Basic State

We now study the process by which a mixture segregates naturally under the effects of gravity and surface tension. We assume that the fluid density ρ_f is less than the matrix density ρ_m ($\Delta\rho = \rho_m - \rho_f > 0$). The process of melt segregation was previously studied [e.g., *Richter and McKenzie*, 1984; *Ribe*, 1987; *Spiegelman*, 1993a, 1993b, 1993c], but with equations including a bulk viscosity. In this section we also retain the viscous stresses in the Navier-Stokes equation for the fluid phase, and we take into account the effects of surface tension assuming near equilibrium conditions; that is, σ is constant and different from zero in (17).

We first look for a steady solution when the mixture is infinite in all directions and has a constant porosity ϕ_0. Gravity $-g\hat{\mathbf{z}}$ is assumed constant and acts in the negative z direction; we also assume the basic state velocities have only z components and are constant.

From (5) we see that the average vertical velocity $\phi v_{f_z} + (1-\phi)v_{m_z}$ is constant. It is therefore appropriate to work in the frame of reference where this average velocity is zero. Since the basic state pressure difference $P_m - P_f$ is only a function of ϕ_0, it is a constant, and (1)-(4) have the solution

$$P_f^0 = -\bar{\rho}gz + \phi_0\sigma\left.\frac{d\alpha}{d\phi}\right|_{\phi_0}, \tag{64}$$

$$P_m^0 = -\bar{\rho}gz - (1-\phi_0)\sigma\left.\frac{d\alpha}{d\phi}\right|_{\phi_0}, \tag{65}$$

$$\mathbf{v}_f^0 = \phi_0(1-\phi_0)^2\frac{\Delta\rho g}{c}\hat{\mathbf{z}}, \tag{66}$$

$$\mathbf{v}_m^0 = -\phi_0^2(1-\phi_0)\frac{\Delta\rho g}{c}\hat{\mathbf{z}}, \tag{67}$$

where $\bar{\rho} = \phi_0\rho_f + (1-\phi_0)\rho_m$ is the average density of the mixture. The superscript zero refers to the basic state with constant porosity. We choose two materially invariant expressions for the pressures, but a common integration constant could been added to the two pressures (since there is no zero reference pressure in an infinite layer). From these expressions we can also define the basic state melt extraction velocity,

$$\mathbf{v}_f - \mathbf{v}_m = \phi_0(1-\phi_0)\frac{\Delta\rho g}{c}\hat{\mathbf{z}}. \tag{68}$$

3.2. Marginal Stability

Let us assume that a perturbation with wave vector $\mathbf{k}$, angular frequency ω, and growth rate s is added to the previous basic state. The net flow is therefore characterized by the quantities

$$q = q^0 + \tilde{q}\ \exp(st)\exp i(\mathbf{k}\cdot\mathbf{u} - \omega t), \tag{69}$$

where the quantities with a tilde are first-order perturbations and where q represents $\mathbf{v}_f$, $\mathbf{v}_m$, P_f, P_m, or ϕ. These expressions are then introduced into (1), (3), (4), (14), and (18). From the matrix mass conservation (2) we get

$$(\omega+is)\tilde{\phi}+(1-\phi_0)\mathbf{k}\cdot\tilde{\mathbf{v}}_m+\phi_0^2(1-\phi_0)k_z\frac{\Delta\rho g}{c}\tilde{\phi}=0, \quad (70)$$

where k_z is the vertical component of $\mathbf{k}$. The sum of mass conservation equations (i.e., (18)) gives

$$\phi_0\mathbf{k}\cdot\tilde{\mathbf{v}}_f+(1-\phi_0)\mathbf{k}\cdot\tilde{\mathbf{v}}_m+\phi_0(1-\phi_0)k_z\frac{\Delta\rho g}{c}\tilde{\phi}=0, \quad (71)$$

the fluid force equation (3) yields,

$$-i\phi_0\mathbf{k}\tilde{P}_f+\Delta\rho g(1-\phi_0)\hat{\mathbf{z}}\tilde{\phi}+c(\tilde{\mathbf{v}}_m-\tilde{\mathbf{v}}_f) \\ -\mu_f\phi_0[k^2\tilde{\mathbf{v}}_f+\frac{1}{3}\mathbf{k}(\mathbf{k}\cdot\tilde{\mathbf{v}}_f)]=0, \quad (72)$$

and the matrix force equation (4) results in

$$-i(1-\phi_0)\mathbf{k}\tilde{P}_m+\Delta\rho g\phi_0\hat{\mathbf{z}}\tilde{\phi}-c(\tilde{\mathbf{v}}_m-\tilde{\mathbf{v}}_f) \\ -\mu_m(1-\phi_0)[k^2\tilde{\mathbf{v}}_m+\frac{1}{3}\mathbf{k}(\mathbf{k}\cdot\tilde{\mathbf{v}}_m)]=0, \quad (73)$$

where $k^2=\mathbf{k}\cdot\mathbf{k}$. Surface tension equilibrium gives

$$\tilde{P}_f-\tilde{P}_m \\ =-\sigma\alpha_0\frac{G(\phi_0)}{\phi_0^2(1-\phi_0)^2}\tilde{\phi}+i\kappa c(\delta_m^2+\delta_f^2) \\ \cdot\left[\mathbf{k}\cdot\tilde{\mathbf{v}}_m-\mathbf{k}\cdot\tilde{\mathbf{v}}_f+k_z(2\phi_0-1)\frac{\Delta\rho g}{c}\right]\tilde{\phi}, \quad (74)$$

where $\delta_f=\sqrt{4\mu_f/3c}$ is the compaction length of the melt, and according to (12) we have defined $G(\phi_0)$ by

$$G(\phi_0)=\phi_0^a(1-\phi_0)^b \\ \cdot[a(1-a)+(a+b-1)(2a-(a+b)\phi_0)\phi_0]. \quad (75)$$

The factor on the right of (75) in brackets is positive definite within the intervals $0\le a,b,\phi\le 1$ since it has one extremum $ab/(a+b)$ at $\phi_0=a/(a+b)$ and has the values $a(1-a)$ and $b(1-b)$ when $\phi_0=0$ and 1, respectively; therefore $G(\phi_0)$ is positive for any exponents a and b between 0 and 1.

We have already seen in the introduction (see also BRS1) that the value $\phi_c=a/(a+b)$ corresponds to a porosity at which the matrix-fluid (or solid-melt) interface changes from concave (relative to the fluid) to convex; this porosity threshold corresponds to a dihedral angle of 60° [*Kohlstedt*, 1992]. However, the value ϕ_c is not associated with any particularly special value of $G(\phi)$; that is, $G(\phi)$ does not change sign at $\phi=\phi_c$ and is not even extremum at this value. Thus the macroscopic dynamics of the mixture does not change when the porosity crosses ϕ_c.

In order to solve (70)-(74) we first find the inner product of the wave vector $\mathbf{k}$ with (72) and (73). The marginal stability problem leads to the dispersion relation

$$\omega = \phi_0(1-\phi_0)\frac{\Delta\rho g}{c}\mathbf{k}\cdot\hat{\mathbf{z}} \cdot \frac{2(1-2\phi_0)-\phi_0(1-\phi_0)k^2(\phi_0^2\delta_m^2-(1-\phi_0)^2\delta_f^2)}{1+\phi_0(1-\phi_0)k^2((\kappa+\phi_0)\delta_m^2+(1+\kappa-\phi_0)\delta_f^2)}, \quad (76)$$

$$s = \frac{\sigma\alpha_0}{c} \cdot \frac{G(\phi_0)k^2}{1+\phi_0(1-\phi_0)k^2((\kappa+\phi_0)\delta_m^2+(1+\kappa-\phi_0)\delta_f^2)}. \quad (77)$$

The solutions are therefore traveling waves with an exponentially growing amplitude. The dispersion relation for the wave frequency (76), corresponds to that found by *Spiegelman* [1993a] in the case $K_0 = 0$, $\delta_f = 0$, and $\phi_0 << 1$.

Figure 8a depicts phase velocities of porosity waves $\mathbf{U_{ph}}$ for various porosities (using $\mathbf{k}\cdot\mathbf{U_{ph}} = \omega$ with (76)). The corresponding group velocities, $\mathbf{U_{gr}} = \nabla_{\mathbf{k}}\omega$, which are the velocities of melt packets, are also shown (Figure 8b). All these velocities are normalized by their melt extraction velocity $\hat{\mathbf{z}}\cdot$(68) and plotted as a function of the normalized wave number $k\delta_m$. We have only considered perturbations with a vertical wave vector ($\mathbf{k} = k_z\hat{\mathbf{z}}$). Porosity perturbations with any vertical variation (i.e., $k_z \neq 0$) will propagate vertically. Porosity perturbations that are constant in z will not propagate at all.

Figure 8

At low porosity and small wave number ($k\delta_m,\ \phi_0 << 1$) the porosity waves and the melt packets travel roughly twice as fast as the background extraction velocity (68). At large wave number, porosity waves and melt packets travel at significantly lower velocities than the background field and can even travel downward. An increase in porosity decreases the wave velocity. When ϕ_0 is larger than 0.5, porosity waves and melt packets always propagate downward with respect to the fluid extraction velocity. This suggests that the velocity of a melt packet can decrease with time since its upward motion will be accompanied by a porosity increase according to (77).

We can scale these results with parameters appropriate to spreading ridges ($\delta_m = 8$ km, $\delta_f \sim 0$ km, $\Delta\rho = 500$ kg m^{-3}, $\mu_m = 10^{18}$ Pa s). In this case, $k\delta_m = 50$ would correspond roughly to a wavelength of 1000 m. The extraction velocities (68) would be 145, 1211, and 1816 mm yr^{-1} for porosities of 0.02, 0.20, and 0.60, respectively.

The fact that the porosity waves always have growing amplitudes is not related to a particular choice of the power law coefficients a and b in (12) since $G(\phi)$ is positive (or $d^2\alpha/d\phi^2 < 0$) for any choice of a and b between 0 and 1. This indicates that surface tension always tends to separate the two phases. The physics is as follows: When two points in the mixture, A and B, have different porosities, they have different average interface curvatures and therefore different surface tensions. Since the difference in sur-

face tension $\sigma[(d\alpha/d\phi)_A - (d\alpha/d\phi)_B]$ always has the opposite sign to the difference in porosity $\phi_A - \phi_B$ (given that $d^2\alpha/d\phi^2 < 0$), the difference in fluid pressure (relative to the matrix pressure) $(P_f - P_m)_A - (P_f - P_m)_B$ also has the opposite sign to $\phi_A - \phi_B$, which indicates a fluid flow toward regions of higher porosity.

Equation (77) is independent of $\Delta\rho$; surface tension induces a self-separation of the two phases without any influence of gravity. Figure 9 shows the normalized growth time of the surface tension instabilities $(3\sigma\alpha_0)/(4s\mu_m)$. The surface tension instability does not select a preferred wavelength. However, short-wavelength instabilities grow the fastest since over short distances it is not energetically difficult to overcome the Darcy resistance and to draw fluid from the surroundings.

Figure 9

The surface tension between solid silicates and their melts σ is typically of order 0.1–1.0 J m^{-2} [*Cooper and Kohlstedt*, 1982; *Lasaga*, 1998]. A simple model can help us to choose a value for α_0. Let us consider a cube of mixture of volume L^3 crossed by N tubules of fluid with the same radius d. The porosity of this mixture is of order $\phi \sim N\pi d^2/L^2$, while the interface density is $\alpha = (2N\pi d)/L^2 = (2\phi)/d$. Equation (12) implies that $\alpha = \alpha_0\phi^a$ at low porosity, and therefore that the radius of the tubules decreases with the porosity, $d = 2\phi^{(1-a)}/\alpha_0$. This behavior is in quantitative agreement with experiments [*von Bargen and Waff*, 1986]. Assuming a porosity ϕ of a few percent (i.e., $0.01 \leq \phi \leq 0.05$) for tubules with radius d of 1–100 μm and $a = 1/2$ implies that $\alpha_0 = 2 \times 10^3$ to $5{\times}10^5$ m^{-1}. During magma compaction, the surface tension effects measured by $\sigma\alpha_0$ should therefore take values between 200 J m^{-3} and 500 kJ m^{-3} (the lower value has been used by *Stevenson* [1986]). These values correspond to pressure heads $\sigma\alpha_0/\bar{\rho}g$ of 7 mm and 17 m. For $\mu_m = 10^{18}$ Pa s the normalization factor of Figure 9, $(4\mu_m)/(3\sigma\alpha_0)$, would be 210 Myr and 84 kyr for $\sigma\alpha_0 = 200$ J m^{-3} and $\sigma\alpha_0 = 500$ kJ m^{-3}, respectively. At low porosity, growth times of a few tens of thousands of years thus can be obtained.

The fact that short-wavelength porosity packets travel the slowest while their growth rate is the largest suggests that surface tension can generate geological structures like dikes or sills. The ability of surface tension to generate instabilities does not depend on the fluid viscosity. The fastest growing instabilities of (77) occur when $k\delta_m$ is large, i.e., either at short wavelength or when the Darcy flow is not the limiting factor. For $a = b = 1/2$ this minimum growth time is

$$\frac{1}{s} = \frac{16}{3}(\phi_0 + \kappa)\sqrt{\phi_0(1-\phi_0)}\frac{\mu_m}{\sigma\alpha_0}, \qquad (78)$$

which indicates that only the matrix viscosity is important; highly viscous melts are as unstable with respect to surface tension as are less viscous melts (within the approximation that $\mu_f \ll \mu_m$). In fact, since the melt extraction velocity decreases with μ_f, surface tension will have more time to act with highly viscous fluids than with less viscous ones. (The surface tension instability is also an integral part of the

shear localization instability and is explored further in the third paper of the series [*Bercovici et al.*, this issue (b)].)

The previous solutions of plane unstable waves are not the only solutions to (70)-(74). If we take $\mathbf{k}\times$ (72) and (73), we find another solution corresponding to flow somewhat related to the Rayleigh-Taylor instability and Rayleigh-Bénard convection. More precisely, a solenoidal (i.e., nondivergent or incompressible) flow is excited and satisfies

$$\mathbf{v}_f = \frac{\Delta\rho g}{c}\,\tilde{\phi}\,(\hat{\mathbf{z}} - \frac{\mathbf{k}\cdot\hat{\mathbf{z}}}{k^2}\mathbf{k}) \cdot \frac{1+\frac{3}{4}(1-\phi_0)^2\delta_m^2 k^2}{(1+\frac{3}{4}(1-\phi_0)\delta_m^2 k^2)(1+\frac{3}{4}\phi_0\delta_f^2 k^2)-1} \quad (79)$$

$$\mathbf{v}_m = \frac{\Delta\rho g}{c}\,\tilde{\phi}\,(\hat{\mathbf{z}} - \frac{\mathbf{k}\cdot\hat{\mathbf{z}}}{k^2}\mathbf{k}) \cdot \frac{1+\frac{3}{4}\phi_0^2\delta_f^2 k^2}{(1+\frac{3}{4}(1-\phi_0)\delta_m^2 k^2)(1+\frac{3}{4}\phi_0\delta_f^2 k^2)-1} \quad (80)$$

The total velocities have both solenoidal components, (79)-(80), and compressible propagating components. The induced solenoidal velocities have zero vertical vorticity $\hat{\mathbf{z}}\cdot(\mathbf{k}\times\mathbf{v}_m) = \hat{\mathbf{z}}\cdot(\mathbf{k}\times\mathbf{v}_f) = 0$; they are purely poloidal.

The solenoidal solutions (79) and (80) are nonzero only if the buoyancy torque $\Delta\rho g\,\mathbf{k}\times\hat{\mathbf{z}}$ is nonzero (i.e, when $\mathbf{k}$ has a horizontal component). Thus unlike porosity waves that are driven by perturbations with vertical wave vectors, this poloidal/solenoidal motion is sensitive to horizontal perturbations of density, just as in ordinary Rayleigh-Bénard convection or the Rayleigh-Taylor instability. Horizontal variations of porosity, and thus of density, induce vertical motions. Regions of low density rise, but the two phases have different upward velocities.

The vertical components of the solenoidal velocities normalized by the melt extraction velocity (68) are depicted in Figure 10. At large wave number, only the fluid moves and the fluid velocities are comparable to $\tilde{\phi}/\phi_0$ times the extraction velocity (see (79) when $k\to\infty$). At very small wave number the Darcy term forces the velocities of the matrix and the fluid to become equal.

Figure 10.

3.3. Nonlinear Solutions of the Compaction Problem

Although the simple marginal stability analysis already shows the complexity of two-phase flows, it is clear that a natural process will be affected by all the nonlinearities of the equations. When all the complexities of the equations are taken into account, the porosity packets $\tilde{\phi}$ will interact with the background flow.

We again examine the compaction problem but in the nonlinear regime. We restrict the equations to one dimension, although we are aware that their solutions may be unstable in three dimensions [*Scott and Stevenson*, 1986; *Barcilon and Lovera*, 1989]. The mixture is confined to a layer of thickness l_0, which contains a matrix with initial volume fraction $1-\phi_0$ and a lighter fluid phase with volume fraction ϕ_0.

On the top and bottom of the layer the matrix and fluid velocities are zero. The equations to solve are the mass conservation equation (18), the porosity evolution equation (2), the action-reaction equation (8) assuming $\underline{\tau}_f = 0$, and the pressure jump condition (17).

Assuming purely vertical flow, using (18) (with the impermeable boundary conditions) to write $\Delta v_z = v_{m_z}/\phi$, and normalizing z by l_0 and v_{m_z} by $(3\rho_m g l_0^2)/(4\mu_m)$, we obtain

$$\phi\left\{\kappa(1-\phi)\frac{\partial}{\partial z}\left[\frac{1}{\phi(1-\phi)}\frac{\partial(1-\phi)v_{m_z}}{\partial z}\right] + \frac{\partial}{\partial z}\left[(1-\phi)\frac{\partial v_{m_z}}{\partial z}\right]\right\} - \xi\frac{G(\phi)}{\phi(1-\phi)}\frac{\partial\phi}{\partial z} - \lambda\frac{v_{m_z}}{\phi} - \phi(1-\phi)\frac{\Delta\rho}{\rho_m} = 0, \qquad (81)$$

where

$$\xi = \frac{\sigma\alpha_0}{\rho_m g l_0} \qquad (82)$$

$$\lambda = \frac{l_0^2}{\delta_m^2}. \qquad (83)$$

Porosity evolution is still controlled by (2) which retains its form even with the normalizations of z and t.

Equation (81) is solved numerically by a finite difference method with a tridiagonal solver. The porosity is then advanced by a time adaptive explicit method. We consider cases (1) with surface tension but no buoyancy forces, (2) without surface tension but with buoyancy, and (3) with both surface tension and buoyancy. In all cases, we assume for simplicity that $a = b = 1/2$ in the surface tension expression (12) and that $\kappa = 3/4$ (i.e., $K_0 = 1$). Clearly, the behavior of the various solutions depends on the relative importance of the Darcy term v_{m_z}/ϕ and the viscous term proportional to λ.

3.3.1. Surface tension without gravity. This type of solution will be also discussed by *Bercovici et al.* [This issue (b)] in connection with damage theory. However, it is also necessary to show here the essential effects of surface tension.

From the stability analysis we know that the wavelengths shorter than the compaction length are the most unstable. When the Darcy term is not the limiting factor, $\delta_m = +\infty$ or $\lambda << 1$, only short wavelengths are effectively present, and all are equally unstable. Figure 11 shows the evolution of the solution initiated with a single long-wavelength perturbation $\phi = 0.05 + 0.001\sin(\pi z/l_0)$. We use 201 finite difference grid points which are sufficient for stable convergence. The rather uniform initial porosity evolves into a single narrow sill of pure fluid.

Figure 11

The previous solution, obtained by neglecting the Darcy term under the assumption that $\lambda << 1$, cannot hold very long. As the porosity decreases on the sides of the high-porosity instability, the importance of the Darcy term increases, and in the end, it dominates the dynamics. In the

extreme case where $\lambda >> 1$, the porosity conservation (2) and (81) can be recast as

$$\frac{\partial \phi}{\partial t} = -\xi \frac{\partial}{\partial z}\left[G(\phi)\frac{\partial \phi}{\partial z}\right]. \qquad (84)$$

The porosity obeys a diffusion equation with a variable and negative diffusivity $D = -\xi G(\phi)$ [see also *Stevenson*, 1986]. With our equations this process occurs at all porosities and indicates that surface tension acts to unmix or separate the two phases whatever their respective proportions. The situation may be different with silicate melts where a contribution to the surface energy comes from grain-grain interfaces [*Riley et al.*, 1990].

A negative diffusivity corresponds to a very unstable process, causing just the reverse evolution of normal diffusion. In this regard, the only thing one learns from numerical solutions to (84) is that any initial condition results in a random distribution of layers where ϕ equals either 1 or 0.

It is therefore more interesting to study intermediate solutions where both viscous and Darcy terms are kept. Figure 12 shows the evolution of the solution initiated by the same long-wavelength perturbation as in Figure 11 but with $\lambda = 4$. The fluid now drains into a number of small sills primarily because the Darcy resistance prohibits the fluid from being drawn across large distances; less energy is therefore used in generating multiple instabilities than in generating one large one (which would pull fluid across the entire depth of the layer).

Figure 12

3.3.2. Gravitational settling without surface tension. As in section 3.3.1, we can define two extreme regimes according to whether the gravity term is balanced by the viscous term or the Darcy term.

In the case where the matrix viscous term is dominant, $\lambda << 1$, the fluid can easily be extracted from a large distance. This is confirmed by the simulation depicted in Figure 13. In the opposite case where the Darcy term is dominant $\lambda >> 1$, the matrix velocity is given by $-\phi^2(1-\phi)(\Delta\rho/\rho_m)\hat{\mathbf{z}}$ analogous to (67). Porosity conservation becomes

Figure 13

$$\frac{\partial \phi}{\partial t} + 2\frac{\Delta\rho}{\rho_m}\phi(1-\phi)(1-2\phi)\frac{\partial \phi}{\partial z} = 0, \qquad (85)$$

which is a nonlinear propagation equation for a porosity wave of phase velocity $2(\Delta\rho/\rho_m)\phi(1-\phi)(1-2\phi)$. This phase velocity is in agreement with (76). Porosity waves propagate upward or downward depending on whether ϕ is greater than or less than $1/2$ (although the fluid always flows upward). The nonlinearity of the phase velocity makes the extraction of the fluid difficult. In the rear of a porosity packet ($\phi < 1/2$ and $\partial\phi/\partial z > 0$) the porosity decreases, $\partial\phi/\partial t < 0$, and this draining of the matrix hampers the propagation of the next rising porosity packet.

In the absence of a viscous term the direct relation between velocity and porosity forbids the imposition of boundary conditions on v_{m_z}. Therefore, in Figure 14 we depict an intermediate case where both viscous and Darcy terms

Figure 14

are kept. The fluid migrates toward the surface but much more slowly than in Figure 13. As the fluid cannot be drawn from a distance much larger than the compaction length, the porosity decreases more or less uniformly below a shallow layer very rich in fluid. Porosity packets called magmons are also generated at depth and travel in the mixture [*Scott and Stevenson*, 1986; *Barcilon and Lovera*, 1989; *Spiegelman*, 1993b].

3.3.3. General case. As seen with (81), surface tension forces balance gravity (assuming $\phi << 1$) when

$$l_0 = \frac{a(1-a)}{\phi^{1-a}} \frac{\sigma\alpha_0}{\Delta\rho g}, \tag{86}$$

i.e., either over a very short distance (in which case the buoyant stress $\Delta\rho g l_0$ is small) or when the porosity is very low (in which case the average interface curvature $d\alpha/d\phi$, and thus the surface tension force, is large). For modeling in a ridge context we can take $(\sigma\alpha_0)/(\Delta\rho g)$ between 40 mm and 100 m for $\sigma\alpha_0 = 200$ J m^{-3} and $\sigma\alpha_0 = 500$ kJ m^{-3}, respectively. ($\Delta\rho = 500$ kg m^{-3}, $\rho_m = 3000$ kg m^{-3}). This implies that surface tension only acts on a scale of a few hundred meters at most.

To show that surface tension can be an important source of instabilities, we perform the computation for a layer of thickness 50 m and a compaction length $\delta_m = 8000$ m. We start with a porosity $\phi = \phi_0[1 - 0.5\cos(2\pi z/l_0)]$, where $\phi_0 = 0.01$. Assuming that the marginal stability analysis remains valid, the porosity waves should slowly drift upward ($U_{ph} = 0.71$ mm yr^{-1} according to (76)), the matrix should compact ($v_{m_z} = -0.74$ mm yr^{-1} according to (67)) and the fluid should flow upward ($v_{f_z} = 74$ mm yr^{-1} according to (66)). Because of surface tension the wave amplitudes should increase with time, and the porosity should reach zero after a time of order $1/s$ (see (78)). After this time the continuity of the flow is interrupted, and sills form. If we take $(\sigma\alpha_0)/(\Delta\rho g)$ between 40 mm and 100 m, growth times shorter than 24 Myr and longer than 24 kyr are obtained (see (78)). In the next simulations we use $\sigma\alpha_0 = 50$ kJ m^{-3}, which lies in the range of values estimated in section 3.2. This should lead to a local draining of the matrix after ∼200 kyr.

Figure 15

In Figure 15 the time evolves from left to right and the porosity (horizontal axis) is plotted as a function of height. From Figure 15a to Figure 15b, the porosity wave moves slowly upward. The nonlinearity of the equations generates harmonics that start propagating at different velocities. At $t = 220$ kyr (between Figures 15b and 15c) the fluid is totally squeezed out from the matrix near the bottom, and the continuity of the flow is interrupted. Then a sill develops by a progressive draining of the matrix mostly from the bottom of the sill (Figures 15d to 15k). The top of the sill also migrates slightly downward. At large time, (Figure 15k) the complete unmixing of the two phases leaves a fluid sill of thickness 1 m.

The time needed to squeeze out the fluid varies qualitatively as predicted by (78), i.e., proportionally to $\mu_m/(\sigma\alpha_0)$.

With the conservative values that we have chosen, this is already short compared to most plate tectonics processes. However, α_0 could be further increased by a factor 10 while the matrix viscosity could be decreased by many orders of magnitude (*Ahern and Turcotte* [1979] and *Turcotte and Phipps Morgan* [1992] consider $\mu_m = 10^{15} - 10^{18}$ Pa s). Therefore, draining times as small as a few 10 years are possible.

As seen in section 3.2, surface tension tends to select the smallest wavelengths. Porosity evolution in a layer of thickness $l_0 = \delta_m = 8000$ m is depicted in Figure 16. The finite difference code in this simulation uses 2000 points, and the initial porosity is a periodic random function with an average value $\phi_0 = 0.01$ and an amplitude spectrum decreasing as $1/k$, where k is the wave number. Except for l_0, the other parameters are similar to those of Figure 15, and periodic boundary conditions are also applied. From Figures 16a-16k we see the upward migration of the various porosity peaks. These peaks deform as they contain different harmonics moving at different phase velocities and because their amplitudes increase. Around $t = 100$ kyrs (Figure 16f), the continuity of the flow is interrupted and various sills start to form. Although long-wavelength components are present in the initial porosity profile, they do not impose the periodicity of the final distribution of sills (Figure 16k). The selected wavelengths result from a compromise between the harmonic content of the initial porosity and a growth rate that favors short wavelengths.

Figure 16

4. Conclusions

In this paper we have investigated fundamental problems of compaction using a new two-phase theory that is materially invariant, includes interfacial surface energy (e.g., surface tension), and accounts for differences in the pressures of the two phases instead of employing a bulk viscosity. Although the bulk viscosity approach (M84) employed in various prior studies is analogous to compressible fluid mechanics formulations, it is meant to model compaction not compressibility; nevertheless, it prescibes compactibility of the matrix through an extra rheological property, i.e., the bulk viscosity ζ. In BRS, no bulk viscosity is employed and the rheological laws remain simple, yet fluid and matrix pressures are assumed unequal as soon as there is some phase separation. This interpretation is very similar to that given by *Scott and Stevenson* [1986] in their Appendix B (although in the main body of the paper they use a constant bulk viscosity as is also assumed in much of M84).

When the porosity is variable, there is no obvious transformation in which a bulk viscosity as per M84 can be inferred from BRS. However, in simple cases of constant and uniform porosity the M84 bulk viscosity approach and the BRS pressure difference effect can be related assuming the bulk viscosity $\zeta \sim \mu_m/\phi$ (see section 2.4.1 and Appendix A).

We believe that our interpretation possibly has some advantages with respect to previous formulations:

1. BRS is materially invariant, that is the equations are perfectly symmetric or invariant to permutations of the subscripts m and f (and implicitly ϕ and $1-\phi$) as should be expected. Use of M84's bulk viscosity approach while maintaining material invariance would require that the fluid also have a bulk viscosity, in which case the mixture of incompressible fluids would lead to a compressible one (BRS1). However, M84 is explicitly for a system that is not materially invariant (i.e., the fluid is always much less viscous than the matrix).

2. With our equations the macroscopic rheology of the mixture becomes that of the end-member single phases when $\phi = 0$ or $\phi = 1$. This is not the case with theories using bulk viscosity, unless mass conservation equations are also invoked; this difficulty prompted various authors to invoke an empirical $\zeta(\phi)$ relationship such that $\zeta \rightarrow +\infty$ when $\phi \rightarrow 0$ (and also when $\phi \rightarrow 1$) [e.g., *McKenzie*, 1984; *Schmeling*, 2000]. When a constant bulk viscosity is used in M84, we have shown in section 2.4 (radial compaction) that the porosity can decrease below zero. The porosity remains strictly between 0 and 1 with BRS.

3. BRS uses the actual matrix and fluid shear viscosities but not the less constrained parameter ζ. Although ζ is generally taken to be equal to μ_m [e.g., *Spiegelman*, 1993c] we have seen in section 2.3 that the choice of ζ smaller than μ_m [e.g., *McKenzie and Holness*, 2000] leads to the unexpected result that the matrix can compact under extensional stresses. In contrast, the parameter K_0 which controls deformation under isotropic stresses in BRS (as does ζ when using M84; see section 2.4.1) can be computed from the topology of the interfaces (see BRS1). That K_0 is expected to be close to unity precludes matrix compaction under extensional stresses in the BRS theory.

We have purposely used simple models to discuss the macroscopic equivalent properties of a two-phase mixture. Various thought experiments have shown that an unconfined mixture is weaker under normal stress than it is under shear stress and that a partially confined mixture can behave like a dashpot with stress hardening properties. The results have been established on clear physical grounds, and in some cases they are different from those previously obtained. In particular, it is more difficult to extract the fluid phase with BRS than with M84 (with constant bulk viscosity). In section 2.3 we have seen that at vanishing porosity the fluid phase is trapped in the matrix with BRS but can still escape with M84 (again, with constant bulk viscosity).

The presence of surface tension has only been discussed in the framework of compaction. It only acts on relatively short distances, and therefore it has been generally neglected in large-scale modeling. However, with all the nonlinearities of the equations the creation of a small-scale instability can impede the further propagation of the fluid phase by drawing in the surrounding fluid yielding a preponderance of stationary sills rather than propagating magmons (magma solitary waves). Indeed, the resulting distribution of sills is reminiscent of the observations of ubiquitous sills and dikes in

ophiolite massifs [*Nicolas et al.*, 1994; *Cannat and Lécuyer*, 1991]. There are large uncertainties in the time constant of this phenomenon but it is likely to be short compared to geologic time. In its present form, our model of surface tension cannot take into account the surface energy associated with solid-solid contacts. This can modify the physics of the system at very low porosity, but as soon as the solid grains are wetted by the fluid, our model should apply.

Direct applications to geophysics, from oil to melt extraction and from core-mantle to outer core-inner core segregation are numerous, although beyond the scope of this paper. The importance of these phenomena make an understanding of the basic physics of the equations a prerequisite to performing complex simulations.

Appendix A: A Comparison Between M84 and BRS

McKenzie [1984] (M84) proposed the following fluid and matrix force equations:

$$-\phi\left[\boldsymbol{\nabla}P + \rho_f g\hat{\mathbf{z}}\right] + c\Delta\mathbf{v} + \boldsymbol{\nabla}\cdot\left[\phi\underline{\boldsymbol{\tau}}_f^*\right] = 0, \tag{A1}$$

$$-(1-\phi)\left[\boldsymbol{\nabla}P + \rho_m g\hat{\mathbf{z}}\right] - c\Delta\mathbf{v} + \boldsymbol{\nabla}\cdot\left[(1-\phi)\underline{\boldsymbol{\tau}}_m^*\right] = 0. \tag{A2}$$

These equations differ from those of BRS (see equations (3) and (4)) by the absence of surface tension ($\sigma = 0$) and and the assumption of a single pressure field, $P_m = P_f = P$, or $\Delta P = 0$. Equations (A1) and (A2) are augmented by the rheological relations

$$\phi\underline{\boldsymbol{\tau}}_f^* \approx 0, \tag{A3}$$

$$\underline{\boldsymbol{\tau}}_m^* = \mu_m^*\left(\boldsymbol{\nabla}\mathbf{v}_m + [\boldsymbol{\nabla}\mathbf{v}_m]^t\right) + (\zeta - \frac{2}{3}\mu_m^*)\boldsymbol{\nabla}\cdot\mathbf{v}_m\underline{\mathbf{I}}. \tag{A4}$$

The fluid phase is assumed inviscid relative to the matrix, and the viscosities μ_m^* and ζ are effective viscosities.

When ϕ is variable, M84 and BRS yield two different sets of equations; in particular, the fluid momentum equation (3) in BRS (again with μ_f negligible) yields

$$-\phi\left[\boldsymbol{\nabla}P_f + \rho_f g\hat{\mathbf{z}}\right] + c\Delta\mathbf{v} = K_0\frac{\mu_m}{(1-\phi)}\frac{\bar{D}\phi}{Dt}\boldsymbol{\nabla}\phi. \tag{A5}$$

The usual modified Darcy's law from M84 ((A1) with (A3)) is thus not recovered by BRS unless the porosity is constant in space and/or time; (A5) expresses the fact that fluid pressure gradients must balance forces associated with compaction of a nonuniform matrix, as well as resistance to interstitial (Darcy) fluid flow.

In the special case where ϕ is constant and uniform, there is a simple correspondence between M84 and BRS. Using the pressure jump condition (17), equations (3) and (4) of BRS become (with μ_f negligible)

$$-\phi\left[\boldsymbol{\nabla} P_f + \rho_f g\hat{\mathbf{z}}\right] + c\Delta\mathbf{v} = 0, \tag{A6}$$

$$-(1-\phi)\left[\boldsymbol{\nabla} P_f + \rho_m g\hat{\mathbf{z}}\right] - c\Delta\mathbf{v} + \boldsymbol{\nabla}\cdot\left[(1-\phi)(\underline{\boldsymbol{\tau}}_m + \frac{K_0}{\phi}\mu_m \boldsymbol{\nabla}\cdot\mathbf{v}_m\underline{\mathbf{I}})\right] = 0. \tag{A7}$$

These equations are identical to (A1) and (A2) with (A3) and (A4) when $P = P_f$, $\mu_m^* = \mu_m$, and $\zeta = K_0\mu_m/\phi$, and we use (9) for $\underline{\boldsymbol{\tau}}_m$. However, even when a formal identification between M84 and BRS can be done, the physical approaches remain significantly different.

Acknowledgments. This work benefited from invaluable discussions with Dan McKenzie and Harro Schmeling. Support was provided by NSF (grant EAR-9458405), the Centre National de la Recherche Scientifique (CNRS), the Institut National des Sciences de l'Univers (INSU) and NASA (HPCC grant NCCS5-147).

References

Ahern, J.L., and D.L. Turcotte, Magma migration beneath an ocean ridge, *Earth Planet. Sci. Lett.*, *45*, 115-122, 1979.

Barcilon, V., and O.M. Lovera, Solitary waves in magma dynamics, *J. Fluid Mech.*, *204*, 121-133, 1989.

Batchelor, G.K., *An Introduction to Fluid Dynamics*, Cambridge Univ. Press, New York,1967.

Bercovici, D., Y. Ricard, and G. Schubert, A two-phase model for compaction and damage, 1, General theory, *J. Geophys. Res.*, this issue (a).

Bercovici, D., Y. Ricard, and G. Schubert, A two-phase model for compaction and damage, 3, Applications to shear localization and plate boundary formation, *J. Geophys. Res.*, this issue (b).

Cannat, M., and C. Lécuyer, Ephemeral magma chambers in the Trinity peridotite, northern California, *Tectonophysics*, *186*, 313-328, 1991.

Cooper, R.F., and D.L. Kohlstedt, Interfacial energies in the olivine-basalt system, in *High Pressure Research in Geophysics*, *Adv. Earth Planet. Sci.*, vol. 12, edited by S. Akimoto and M. H. Manghnani, pp. 217-228, Cent. for Acad. Pub., Tokyo, 1982.

Drew, D. A., Averaged field equations for two-phase flow, *Annu. Rev. Fluid Mech.*, *15*, 261-291, 1983.

Drew, D.A., and S.L. Passman, *Theory of Multicomponent Fluids*, Appl. Math. Sci., vol.135, Springer-Verlag, New York, 1999.

Farren, W.S., and G.I. Taylor, The heat developed during plastic extension of metals, *Proc. R. Soc. London, Ser. A, 107*, 422–451, 1925.

Fowler, A.C., A compaction model for melt transport in the Earth's asthenosphere, part I, The basic model, in *Magma Transport and Storage*, edited by M.P. Ryan, ed., pp. 3-14, John Wiley, New York, 1990a.

Fowler, A.C., A compaction model for melt transport in the Earth's asthenosphere, part II, Applications, in *Magma Transport and Storage*, edited by M.P. Ryan, ed., pp. 15-32, John Wiley, New York, 1990b.

Kohlstedt, D. L., Structure, rheology and permeability of partially molten rocks at low melt fractions, in, *Mantle Flow and Melt-Generation at Mid-Ocean Ridges, Geophys. Monogr. Ser.*, vol. 71, edited by J. Phipps Morgan, D.K. Blackman and J.M. Sinton, pp. 103-121, AGU, Washington, D. C., 1992.

Landau, L.D., and E.M. Lifshitz, *Fluid Mechanics, Course Theoret. Phys.*, vol. 6, Pergamon, New York, 1959.

Lasaga, A.C., *Kinetic Theory in the Earth Sciences*, Princeton Univ. Press, Princeton, N. J., 1998.

McKenzie, D., The generation and compaction of partially molten rocks, *J. Petrol., 25*, 713-765, 1984.

McKenzie, D., The extraction of magma from the crust and mantle, *Earth Planet. Sci. Lett., 74*, 81-91, 1985.

McKenzie, D., The compaction of igneous and sedimentary rocks, *J. Geol. Soc. London, 144*, 299-307, 1987.

McKenzie, D., and M. Holness, Local deformation in compacting flows: Development of pressure shadows, *Earth Planet. Sci. Lett., 180*, 169-184, 2000.

Ni, J., and C. Beckermann, A volume-averaged two-phase model for transport phenomena during solidification, *Metall. Trans. B, 22*, 349-361, 1991.

Nicolas A., F. Boudier, and B. Ildefonse, Dike patterns in diapirs beneath oceanic ridges: The Oman ophiolite, in *Magmatic Systems*, edited by M. P. Ryan, pp. 77-95, Academic, San Diego, Calif., 1994.

O'Connell, R. J., and B. Budiansky, Viscoelastic properties of fluid saturated cracked solids, *J. Geophys. Res., 82*, 5719-5735, 1977.

Ribe, N.M., The deformation and compaction of partial molten zones, *Geophys. J. R. Astron. Soc., 83*, 487-501, 1985.

Ribe, N.M., Theory of melt segregation-A review, *J. Volcanol. Geotherm. Res., 33*, 241-253, 1987.

Richter, F.M., and D. McKenzie, Dynamical models for melt segregation from a deformable matrix, *J. Geol., 92*, 729-740, 1984.

Riley, G.N., Jr., and D.L. Kohslstedt, Kinetics of melt migration in upper mantle-type rocks, *Earth Planet. Sci. Lett., 105*, 500-521, 1991.

Riley, G.N., Jr., D.L. Kohslstedt and F.M. Richter, Melt migration in a silicate liquid-olivine system: An experimental test of compaction theory, *Geophys. Res. Lett., 17*, 2101-2104, 1990.

Schmeling, H., Numerical models on the influence of partial melt on elastic, anelastic, and electric properties of rocks, part 1, Elasticity and anelasticity, *Phys. Earth Planet. Inter., 41*, 34-57, 1985.

Schmeling, H., Partial melting and melt segregation in a convecting mantle, in *Physics and Chemistry of Partially Molten Rocks*, edited by N. Bagdassarov, D. Laporte, and A.B. Thompson, Kluwer Acad., Norwell, Mass., pp. 141-178, 2000.

Scott, D.R., and D.J. Stevenson, Magma solitons, *Geophys. Res. Lett., 11*, 1161-1164, 1984.

Scott, D.R., and D.J. Stevenson, Magma ascent by porous flow, *J. Geophys. Res., 91*, 9283-9296, 1986.

Spiegelman, M., Flow in deformable porous media, part 1, Simple analysis, *J. Fluid Mech., 247*, 17-38, 1993a.

Spiegelman, M., Flow in deformable porous media, part 2, Numerical analysis- The relationship between shock waves and solitary waves, *J. Fluid Mech., 247*, 39-63, 1993b.

Spiegelman, M., Physics of melt extraction: Theory, implications and applications, *Philos. Trans. R. Soc. London. Ser. A, 342*, 23-41, 1993c.

Stevenson, D.J., On the role of surface tension in the migration of melts and fluids, *Geophys. Res. Lett.*, 13, 1149-1152, 1986.

Taylor, G.I., and H. Quinney, The latent energy remaining in metal after cold working, *Proc. R. Soc. London, Ser. A, 143*, 307-326, 1934.

Turcotte, D.L., and J. Phipps Morgan, The physics of magma migration and mantle flow beneath a mid-ocean ridge, in *Mantle Flow and Melt-Generation at Mid-Ocean Ridges, Geophys. Monograph. Ser.*, vol. 71, edited by J. Phipps Morgan, D.K. Blackman, and J.M. Sinton, pp. 155-182, AGU, Washington, D. C., 1992.

von Bargen, N., and H.S. Waff, Permeabilities, interfacial areas and curvatures of partially molten systems: Results of numerical

computations of equilibrium microstructures, *J. Geophys. Res.*, *91*, 9261-9276, 1986.

D. Bercovici, Department of Geology and Geophysics, Yale University, P.O. Box 208109, New Haven, C T 06520-8109. (david.bercovici@yale.edu)

Y. Ricard, Laboratoire des Sciences de la Terre, Ecole Normale Supérieure de Lyon, 46 allée d'Italie, F-69364 Lyon, Cedex 07, France. (ricard@ens-lyon.fr)

G. Schubert, Department of Earth and Space Sciences, University of California, Los Angeles, 595 Circle Drive East, Los Angeles, CA 90095-1567. (schubert@ucla.edu)

(Received November 1, 1999; revised May 18, 2000;
accepted October 31, 2000.)

Copyright 2001 by the American Geophysical Union.

Paper number 2000JB900431.
0148-0227/01/2000JB900431$09.00

RICARD ET AL.: TWO-PHASE COMPACTION AND DAMAGE, 2, COMPACTION

RICARD ET AL.: TWO-PHASE COMPACTION AND DAMAGE, 2, COMPACTION

RICARD ET AL.: TWO-PHASE COMPACTION AND DAMAGE, 2, COMPACTION

RICARD ET AL.: TWO-PHASE COMPACTION AND DAMAGE, 2, COMPACTION

RICARD ET AL.: TWO-PHASE COMPACTION AND DAMAGE, 2, COMPACTION

RICARD ET AL.: TWO-PHASE COMPACTION AND DAMAGE, 2, COMPACTION

RICARD ET AL.: TWO-PHASE COMPACTION AND DAMAGE, 2, COMPACTION

RICARD ET AL.: TWO-PHASE COMPACTION AND DAMAGE, 2, COMPACTION

RICARD ET AL.: TWO-PHASE COMPACTION AND DAMAGE, 2, COMPACTION

RICARD ET AL.: TWO-PHASE COMPACTION AND DAMAGE, 2, COMPACTION

RICARD ET AL.: TWO-PHASE COMPACTION AND DAMAGE, 2, COMPACTION

RICARD ET AL.: TWO-PHASE COMPACTION AND DAMAGE, 2, COMPACTION

RICARD ET AL.: TWO-PHASE COMPACTION AND DAMAGE, 2, COMPACTION

RICARD ET AL.: TWO-PHASE COMPACTION AND DAMAGE, 2, COMPACTION

RICARD ET AL.: TWO-PHASE COMPACTION AND DAMAGE, 2, COMPACTION

RICARD ET AL.: TWO-PHASE COMPACTION AND DAMAGE, 2, COMPACTION

RICARD ET AL.: TWO-PHASE COMPACTION AND DAMAGE, 2, COMPACTION

RICARD ET AL.: TWO-PHASE COMPACTION AND DAMAGE, 2, COMPACTION

RICARD ET AL.: TWO-PHASE COMPACTION AND DAMAGE, 2, COMPACTION

RICARD ET AL.: TWO-PHASE COMPACTION AND DAMAGE, 2, COMPACTION

RICARD ET AL.: TWO-PHASE COMPACTION AND DAMAGE, 2, COMPACTION

RICARD ET AL.: TWO-PHASE COMPACTION AND DAMAGE, 2, COMPACTION

RICARD ET AL.: TWO-PHASE COMPACTION AND DAMAGE, 2, COMPACTION

RICARD ET AL.: TWO-PHASE COMPACTION AND DAMAGE, 2, COMPACTION

RICARD ET AL.: TWO-PHASE COMPACTION AND DAMAGE, 2, COMPACTION

RICARD ET AL.: TWO-PHASE COMPACTION AND DAMAGE, 2, COMPACTION

RICARD ET AL.: TWO-PHASE COMPACTION AND DAMAGE, 2, COMPACTION

RICARD ET AL.: TWO-PHASE COMPACTION AND DAMAGE, 2, COMPACTION

RICARD ET AL.: TWO-PHASE COMPACTION AND DAMAGE, 2, COMPACTION

RICARD ET AL.: TWO-PHASE COMPACTION AND DAMAGE, 2, COMPACTION

RICARD ET AL.: TWO-PHASE COMPACTION AND DAMAGE, 2, COMPACTION

RICARD ET AL.: TWO-PHASE COMPACTION AND DAMAGE, 2, COMPACTION

RICARD ET AL.: TWO-PHASE COMPACTION AND DAMAGE, 2, COMPACTION

RICARD ET AL.: TWO-PHASE COMPACTION AND DAMAGE, 2, COMPACTION

RICARD ET AL.: TWO-PHASE COMPACTION AND DAMAGE, 2, COMPACTION

RICARD ET AL.: TWO-PHASE COMPACTION AND DAMAGE, 2, COMPACTION

RICARD ET AL.: TWO-PHASE COMPACTION AND DAMAGE, 2, COMPACTION

RICARD ET AL.: TWO-PHASE COMPACTION AND DAMAGE, 2, COMPACTION

RICARD ET AL.: TWO-PHASE COMPACTION AND DAMAGE, 2, COMPACTION

RICARD ET AL.: TWO-PHASE COMPACTION AND DAMAGE, 2, COMPACTION

RICARD ET AL.: TWO-PHASE COMPACTION AND DAMAGE, 2, COMPACTION

RICARD ET AL.: TWO-PHASE COMPACTION AND DAMAGE, 2, COMPACTION

RICARD ET AL.: TWO-PHASE COMPACTION AND DAMAGE, 2, COMPACTION

RICARD ET AL.: TWO-PHASE COMPACTION AND DAMAGE, 2, COMPACTION

RICARD ET AL.: TWO-PHASE COMPACTION AND DAMAGE, 2, COMPACTION

RICARD ET AL.: TWO-PHASE COMPACTION AND DAMAGE, 2, COMPACTION

RICARD ET AL.: TWO-PHASE COMPACTION AND DAMAGE, 2, COMPACTION

RICARD ET AL.: TWO-PHASE COMPACTION AND DAMAGE, 2, COMPACTION

RICARD ET AL.: TWO-PHASE COMPACTION AND DAMAGE, 2, COMPACTION

RICARD ET AL.: TWO-PHASE COMPACTION AND DAMAGE, 2, COMPACTION

RICARD ET AL.: TWO-PHASE COMPACTION AND DAMAGE, 2, COMPACTION

RICARD ET AL.: TWO-PHASE COMPACTION AND DAMAGE, 2, COMPACTION

RICARD ET AL.: TWO-PHASE COMPACTION AND DAMAGE, 2, COMPACTION

RICARD ET AL.: TWO-PHASE COMPACTION AND DAMAGE, 2, COMPACTION

RICARD ET AL.: TWO-PHASE COMPACTION AND DAMAGE, 2, COMPACTION

RICARD ET AL.: TWO-PHASE COMPACTION AND DAMAGE, 2, COMPACTION

RICARD ET AL.: TWO-PHASE COMPACTION AND DAMAGE, 2, COMPACTION

Figure Captions

Figure 1. The one-dimensional compaction "coffee-press" experiment.

Figure 1. The one-dimensional compaction "coffee-press" experiment.

Figure 2. Normalized friction coefficient ν/μ_m as a function of porosity for $l_0/\delta_m = 0.1,\ 10$. Our predictions (BRS) are shown by thick lines ($K_0 = 1$). At low porosity the friction coefficient is significantly larger than that predicted by previous theories (dashed lines labeled M84, following (30) with $\zeta = \mu_m$). The friction increases with l_0. This friction coefficient is often much larger than 1, which corresponds to the shear viscosity of the matrix.

Figure 2. Normalized friction coefficient ν/μ_m as a function of porosity for $l_0/\delta_m = 0.1,\ 10$. Our predictions (BRS) are shown by thick lines ($K_0 = 1$). At low porosity the friction coefficient is significantly larger than that predicted by previous theories (dashed lines labeled M84, following (30) with $\zeta = \mu_m$). The friction increases with l_0. This friction coefficient is often much larger than 1, which corresponds to the shear viscosity of the matrix.

Figure 3. (a) Normalized porosity (ϕ/ϕ_0) as a function of normalized height (z/l_0) for different times ($t/\tau = 0.1$, 0.3, 0.5, 0.7 and 0.83) for $(l_0/(\delta_m\phi_0))^2 = 0.1$, $K_0 = 1$, and $\phi_0 = 0.05$. As time increases, the height of the mixture below the piston decreases. (b) Normalized velocity (v_{m_z}/v_0) as a function of normalized height for $t/\tau = 0.1$ and 0.83. Until close to the end of the experiment, the velocity profile remains roughly linear.

Figure 3. (a) Normalized porosity (ϕ/ϕ_0) as a function of normalized height (z/l_0) for different times ($t/\tau = 0.1$, 0.3, 0.5, 0.7 and 0.83) for $(l_0/(\delta_m\phi_0))^2 = 0.1$, $K_0 = 1$, and $\phi_0 = 0.05$. As time increases, the height of the mixture below the piston decreases. (b) Normalized velocity (v_{m_z}/v_0) as a function of normalized height for $t/\tau = 0.1$ and 0.83. Until close to the end of the experiment, the velocity profile remains roughly linear.

Figure 4. Evolution of friction coefficient $\nu(t)/\mu_m$ as a function of time. This coefficient is proportional to the pressure needed to expel the fluid at a constant velocity. When the porosity reaches 0 near $t/\tau = 0.83$, the friction coefficient goes to infinity and forbids a further extraction of the fluid phase. The horizontal dashed line corresponds to the analytical prediction (27).

Figure 4. Evolution of friction coefficient $\nu(t)/\mu_m$ as a function of time. This coefficient is proportional to the pressure needed to expel the fluid at a constant velocity. When the porosity reaches 0 near $t/\tau = 0.83$, the friction coefficient goes to infinity and forbids a further extraction of the fluid phase. The horizontal dashed line corresponds to the analytical prediction (27).

Figure 5. Equivalent viscosity of the mixture as function of porosity for two different values of l_0/δ_m (0.1, 10). Our predictions (BRS) with $K_0 = 1$ are depicted with a solid line and compared with those obtained by previous theories assuming $\zeta = \mu_m$ (dashed lines labeled M84). At small compaction length, e.g., at $l_0/\delta_m = 10$, BRS and M84 predictions are indistinguishable.

Figure 5. Equivalent viscosity of the mixture as function of porosity for two different values of l_0/δ_m (0.1, 10). Our predictions (BRS) with $K_0 = 1$ are depicted with a solid line and compared with those obtained by previous theories assuming $\zeta = \mu_m$ (dashed lines labeled M84). At small compaction length, e.g., at $l_0/\delta_m = 10$, BRS and M84 predictions are indistinguishable.

Figure 6. (top) Horizontal fluid velocities normalized by the vertical velocity v_0 at $x = l_0$ for l_0/δ_m=0.1 using BRS ($K_0 = 1$) or M84 set of equations. When the porosity is zero, the first drop of fluid is expelled with a $\sim$12 times higher velocity according to M84, while the fluid is simply transported along with the matrix according to BRS. The fluid velocity decreases to v_0 when $\phi_0 = 1$. (bottom) Matrix velocities can be negative according to M84 when $\zeta < \mu_m$ (thin line with $\zeta = \mu_m/10$).

Figure 6. (top) Horizontal fluid velocities normalized by the vertical velocity v_0 at $x = l_0$ for l_0/δ_m=0.1 using BRS ($K_0 = 1$) or M84 set of equations. When the porosity is zero, the first drop of fluid is expelled with a $\sim$12 times higher velocity according to M84, while the fluid is simply transported along with the matrix according to BRS. The fluid velocity decreases to v_0 when $\phi_0 = 1$. (bottom) Matrix velocities can be negative according to M84 when $\zeta < \mu_m$ (thin line with $\zeta = \mu_m/10$).

Figure 7. Normalized resistance to compaction $(R\Sigma)/(\mu_m v_{m_r})$ for a spherical mixture of homogeneous porosity, as a function of porosity. The solid lines correspond to our solutions in the sintering approximation (BRS) or with a finite compaction length (BRS with $R/\delta_m = 10$). The dashed line corresponds to the solution given by *McKenzie* [1984] using the sintering approximation and a theory that includes a bulk viscosity ($\zeta = \mu_m$) (see (57)).

Figure 7. Normalized resistance to compaction $(R\Sigma)/(\mu_m v_{m_r})$ for a spherical mixture of homogeneous porosity, as a function of porosity. The solid lines correspond to our solutions in the sintering approximation (BRS) or with a finite compaction length (BRS with $R/\delta_m = 10$). The dashed line corresponds to the solution given by *McKenzie* [1984] using the sintering approximation and a theory that includes a bulk viscosity ($\zeta = \mu_m$) (see (57)).

Figure 8. (a) Phase and (b) group velocities of vertically propagating porosity waves. The velocities are normalized by the melt extraction velocity (68). Three porosities are used 0.02, 0.20, and 0.60. We assume $\delta_f = 0$ and $K_0 = 1$. Small wave number (long wavelength) perturbations travel the fastest.

Figure 8. (a) Phase and (b) group velocities of vertically propagating porosity waves. The velocities are normalized by the melt extraction velocity (68). Three porosities are used 0.02, 0.20, and 0.60. We assume $\delta_f = 0$ and $K_0 = 1$. Small wave number (long wavelength) perturbations travel the fastest.

Figure 9. Normalized growth time of surface tension instabilities as a function of their normalized wave number for $a = b = 1/2$ in $G(\phi_0)$, $K_0 = 1$, $\delta_f = 0$, and $\phi_0 = 0.02, 0.20$ and 0.60, as in Figure 8. All wave numbers are unstable, but shorter-wavelength instabilities grow faster. Because the surface energy tends to $+\infty$ when the porosity vanishes, instabilities grow the fastest at small porosity.

Figure 9. Normalized growth time of surface tension instabilities as a function of their normalized wave number for $a = b = 1/2$ in $G(\phi_0)$, $K_0 = 1$, $\delta_f = 0$, and $\phi_0 = 0.02, 0.20$ and 0.60, as in Figure 8. All wave numbers are unstable, but shorter-wavelength instabilities grow faster. Because the surface energy tends to $+\infty$ when the porosity vanishes, instabilities grow the fastest at small porosity.

Figure 10. Matrix (solid lines) and fluid (dashed lines) vertical velocities of the solenoidal motions. The velocities are normalized by $\phi_0(1-\phi_0)\tilde{\phi}\Delta\rho/c$, i.e., the product of the melt extraction velocities by the amplitude of the porosity perturbation. We assume $\delta_f = 0$ and $\mathbf{k}\cdot\hat{\mathbf{z}} = 0$ and $\tilde{\phi} = 1$. At short wavelength (large wave number) only the fluid is in motion. At long wavelength (short wave number), fluid and matrix velocities become equal.

Figure 10. Matrix (solid lines) and fluid (dashed lines) vertical velocities of the solenoidal motions. The velocities are normalized by $\phi_0(1-\phi_0)\tilde{\phi}\Delta\rho/c$, i.e., the product of the melt extraction velocities by the amplitude of the porosity perturbation. We assume $\delta_f = 0$ and $\mathbf{k}\cdot\hat{\mathbf{z}} = 0$ and $\tilde{\phi} = 1$. At short wavelength (large wave number) only the fluid is in motion. At long wavelength (short wave number), fluid and matrix velocities become equal.

Figure 11. Porosity as a function of depth at different times for $\xi = 1$, $\lambda = 0$, and $\Delta\rho/\rho_m = 0$. The initial porosity has an average value of 0.05 and has a sinusoidal perturbation of wavelength l_0 and amplitude 0.001 with its maximum at $l_0/2$. The surface tension generates the instability. The Darcy term has been neglected. A single instability is produced.

Figure 11. Porosity as a function of depth at different times for $\xi = 1$, $\lambda = 0$, and $\Delta\rho/\rho_m = 0$. The initial porosity has an average value of 0.05 and has a sinusoidal perturbation of wavelength l_0 and amplitude 0.001 with its maximum at $l_0/2$. The surface tension generates the instability. The Darcy term has been neglected. A single instability is produced.

Figure 12. Porosity as a function of depth at different times for $\xi = 1$, $\lambda = 4$, and $\Delta\rho/\rho_m = 0$. The parameters are similar to those of Figure 11, but the Darcy term has been kept. Because of the presence of a Darcy resistance which prohibits the fluid from being drawn across large distances, the number of instabilities increases when compared to Figure 11.

Figure 12. Porosity as a function of depth at different times for $\xi = 1$, $\lambda = 4$, and $\Delta\rho/\rho_m = 0$. The parameters are similar to those of Figure 11, but the Darcy term has been kept. Because of the presence of a Darcy resistance which prohibits the fluid from being drawn across large distances, the number of instabilities increases when compared to Figure 11.

Figure 13. Porosity as a function of depth at different times for $\xi = 0$, $\lambda = 0$ and $\Delta\rho/\rho_m = 1$. The mixture is gravitationally unstable, and there is no surface tension. The matrix viscous term is dominant in the dynamics.

Figure 13. Porosity as a function of depth at different times for $\xi = 0$, $\lambda = 0$ and $\Delta\rho/\rho_m = 1$. The mixture is gravitationally unstable, and there is no surface tension. The matrix viscous term is dominant in the dynamics.

Figure 14. Porosity as a function of depth at different times for $\xi = 0$, $\lambda = 10$, and $\Delta\rho/\rho_m = 1$. The initial porosity is constant. The mixture is gravitationally unstable and without surface tension. Because of the presence of the Darcy term, porosity packets are generated.

Figure 14. Porosity as a function of depth at different times for $\xi = 0$, $\lambda = 10$, and $\Delta\rho/\rho_m = 1$. The initial porosity is constant. The mixture is gravitationally unstable and without surface tension. Because of the presence of the Darcy term, porosity packets are generated.

Figure 15. Time evolution (from (a) 0 years, (b) 120 kyr, (c) 250 kyr, (d) 420 kyr, (e) 620 kyr, (f) 850 kyr, (g) 1.1 Myr, (h) 1.4 Myr, (i) 1.8 Myr, (j) 2.2 Myr, to (k) 16 Myr) of porosity as a function of depth ($K_0 = 1$, $\Delta\rho = 500$ kg m^{-3}, $l_0 = 50$ m, $\delta_m = 8000$ m, $\mu_m = 10^{18}$ Pa s, $\rho_m = 3000$ kg m^{-3}, $\sigma\alpha_0 = 50$ kJ m^{-3}). For clarity,each profile as been x hifted by 0.1 porosity unit with respect to the previous profile. The initial porosity is a sinusoidal function with a maximum at $z/l_0 = 0.5$. The porosity wave travels upward until the surface tension dries the matrix at one point (at $t =$ 140 kyr, i.e., between Figures 15b and 15c). The evolution ultimately generates a sill of pure fluid (Figure 15k).

Figure 15. Time evolution (from (a) 0 years, (b) 120 kyr, (c) 250 kyr, (d) 420 kyr, (e) 620 kyr, (f) 850 kyr, (g) 1.1 Myr, (h) 1.4 Myr, (i) 1.8 Myr, (j) 2.2 Myr, to (k) 16 Myr) of porosity as a function of depth ($K_0 = 1$, $\Delta\rho = 500$ kg m^{-3}, $l_0 = 50$ m, $\delta_m = 8000$ m, $\mu_m = 10^{18}$ Pa s, $\rho_m = 3000$ kg m^{-3}, $\sigma\alpha_0 = 50$ kJ m^{-3}). For clarity,each profile as been x hifted by 0.1 porosity unit with respect to the previous profile. The initial porosity is a sinusoidal function with a maximum at $z/l_0 = 0.5$. The porosity wave travels upward until the surface tension dries the matrix at one point (at $t = 140$ kyr, i.e., between Figures 15b and 15c). The evolution ultimately generates a sill of pure fluid (Figure 15k).

Figure 16. Same as Figure 15 but for a more complex initial porosity over a larger height ($K_0 = 1$, $\Delta\rho = 500$ kg m^{-3}, $l_0 = \delta_m = 8000$ m, $\mu_m = 10^{18}$ Pa s, $\rho_m = 3000$ kg m^{-3}, $\sigma\alpha_0 = 50$ kJ m^{-3}). Although long-wavelength harmonics are present in the starting porosity, the surface tension preferentially selects short wavelengths. The profiles are depicted at times (a) 0,(b) 15, (c) 29, (d) 47, (e) 70, (f) 100, (g) 140, (h) 240, (i) 400, (j) 600 and (k) 900 kyr.

Figure 16. Same as Figure 15 but for a more complex initial porosity over a larger height ($K_0 = 1$, $\Delta\rho = 500$ kg m^{-3}, $l_0 = \delta_m = 8000$ m, $\mu_m = 10^{18}$ Pa s, $\rho_m = 3000$ kg m^{-3}, $\sigma\alpha_0 = 50$ kJ m^{-3}). Although long-wavelength harmonics are present in the starting porosity, the surface tension preferentially selects short wavelengths. The profiles are depicted at times (a) 0,(b) 15, (c) 29, (d) 47, (e) 70, (f) 100, (g) 140, (h) 240, (i) 400, (j) 600 and (k) 900 kyr.

Figures

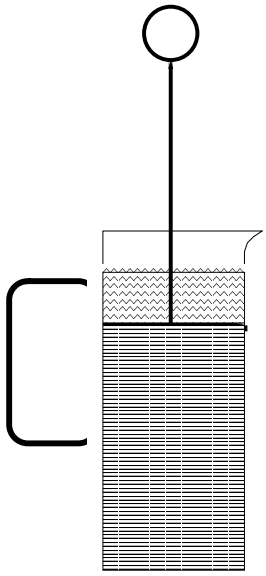

Figure 1. The one-dimensional compaction "coffee-press" experiment.

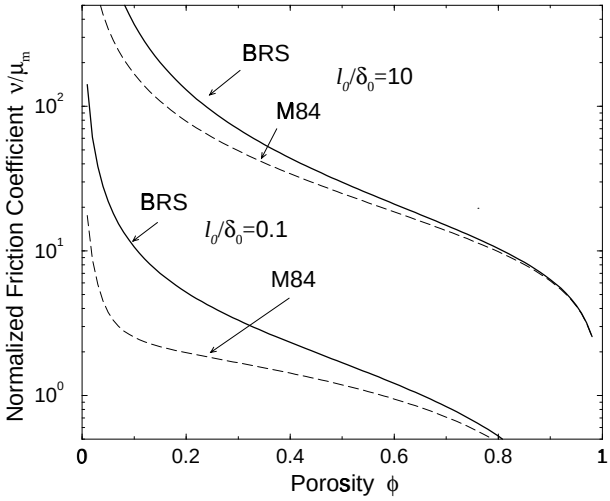

Figure 2. Normalized friction coefficient ν/μ_m as a function of porosity for $l_0/\delta_m = 0.1,\ 10$. Our predictions (BRS) are shown by thick lines ($K_0 = 1$). At low porosity the friction coefficient is significantly larger than that predicted by previous theories (dashed lines labeled M84, following (30) with $\zeta = \mu_m$). The friction increases with l_0. This friction coefficient is often much larger than 1, which corresponds to the shear viscosity of the matrix.

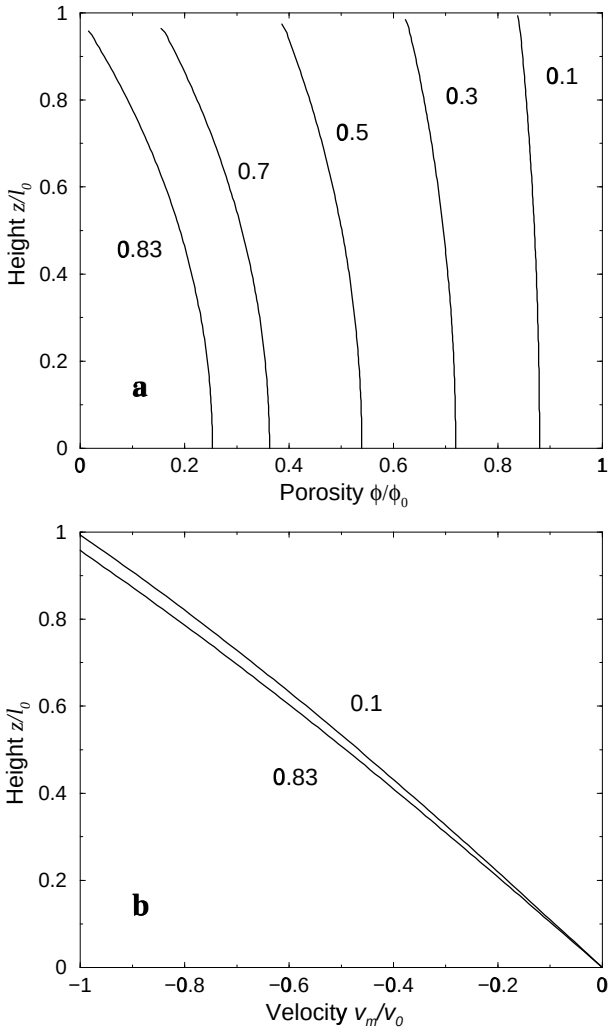

Figure 3. (a) Normalized porosity (ϕ/ϕ_0) as a function of normalized height (z/l_0) for different times ($t/\tau = 0.1$, 0.3, 0.5, 0.7 and 0.83) for $(l_0/(\delta_m\phi_0))^2 = 0.1$, $K_0 = 1$, and $\phi_0 = 0.05$. As time increases, the height of the mixture below the piston decreases. (b) Normalized velocity (v_{m_z}/v_0) as a function of normalized height for $t/\tau = 0.1$ and 0.83. Until close to the end of the experiment, the velocity profile remains roughly linear.

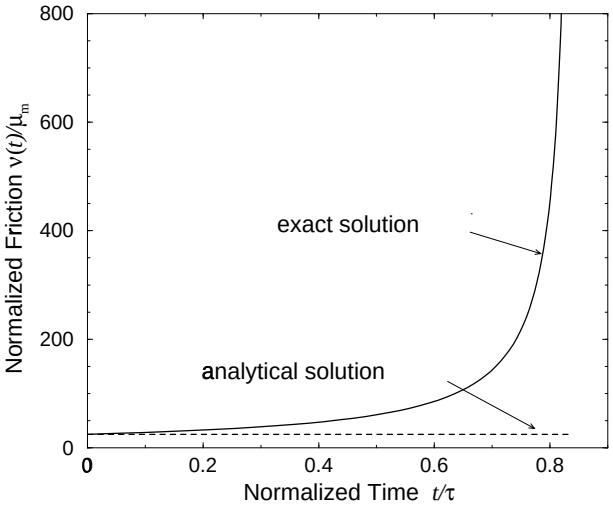

Figure 4. Evolution of friction coefficient $\nu(t)/\mu_m$ as a function of time. This coefficient is proportional to the pressure needed to expel the fluid at a constant velocity. When the porosity reaches 0 near $t/\tau = 0.83$, the friction coefficient goes to infinity and forbids a further extraction of the fluid phase. The horizontal dashed line corresponds to the analytical prediction (27).

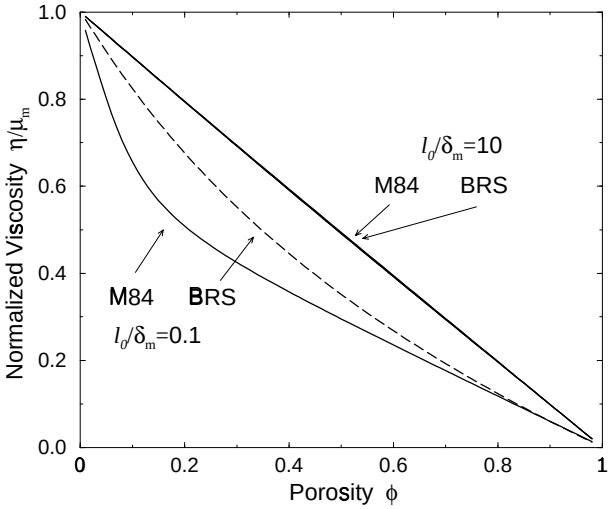

Figure 5. Equivalent viscosity of the mixture as function of porosity for two different values of l_0/δ_m (0.1, 10). Our predictions (BRS) with $K_0 = 1$ are depicted with a solid line and compared with those obtained by previous theories assuming $\zeta = \mu_m$ (dashed lines labeled M84). At small compaction length, e.g., at $l_0/\delta_m = 10$, BRS and M84 predictions are indistinguishable.

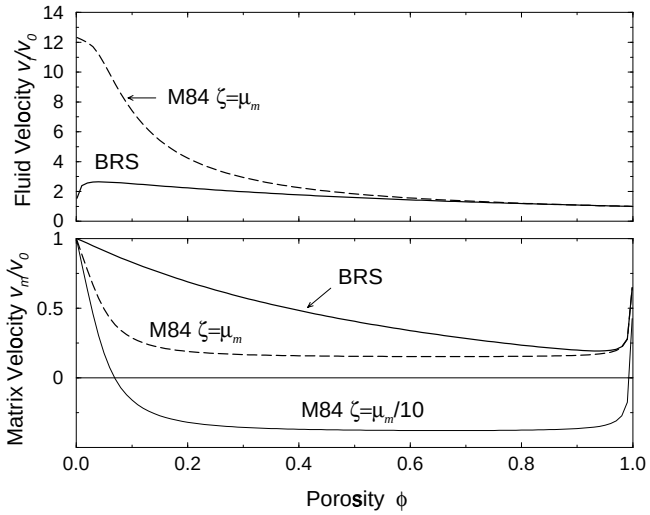

Figure 6. (top) Horizontal fluid velocities normalized by the vertical velocity v_0 at $x = l_0$ for l_0/δ_m=0.1 using BRS ($K_0 = 1$) or M84 set of equations. When the porosity is zero, the first drop of fluid is expelled with a $\sim$12 times higher velocity according to M84, while the fluid is simply transported along with the matrix according to BRS. The fluid velocity decreases to v_0 when $\phi_0 = 1$. (bottom) Matrix velocities can be negative according to M84 when $\zeta < \mu_m$ (thin line with $\zeta = \mu_m/10$).

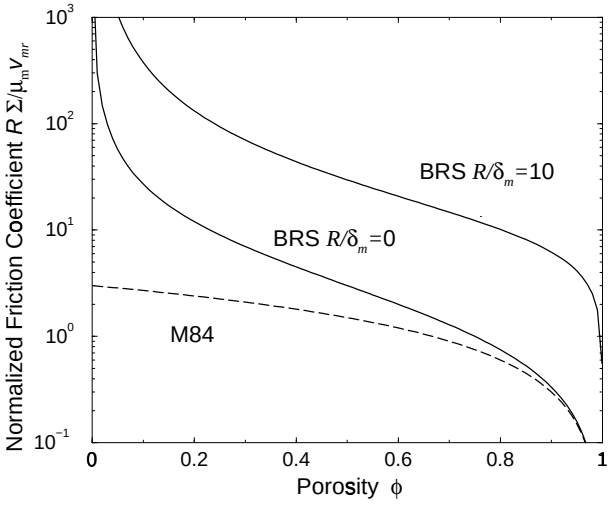

Figure 7. Normalized resistance to compaction $(R\Sigma)/(\mu_m v_{m_r})$ for a spherical mixture of homogeneous porosity, as a function of porosity. The solid lines correspond to our solutions in the sintering approximation (BRS) or with a finite compaction length (BRS with $R/\delta_m = 10$). The dashed line corresponds to the solution given by *McKenzie* [1984] using the sintering approximation and a theory that includes a bulk viscosity ($\zeta = \mu_m$) (see (57)).

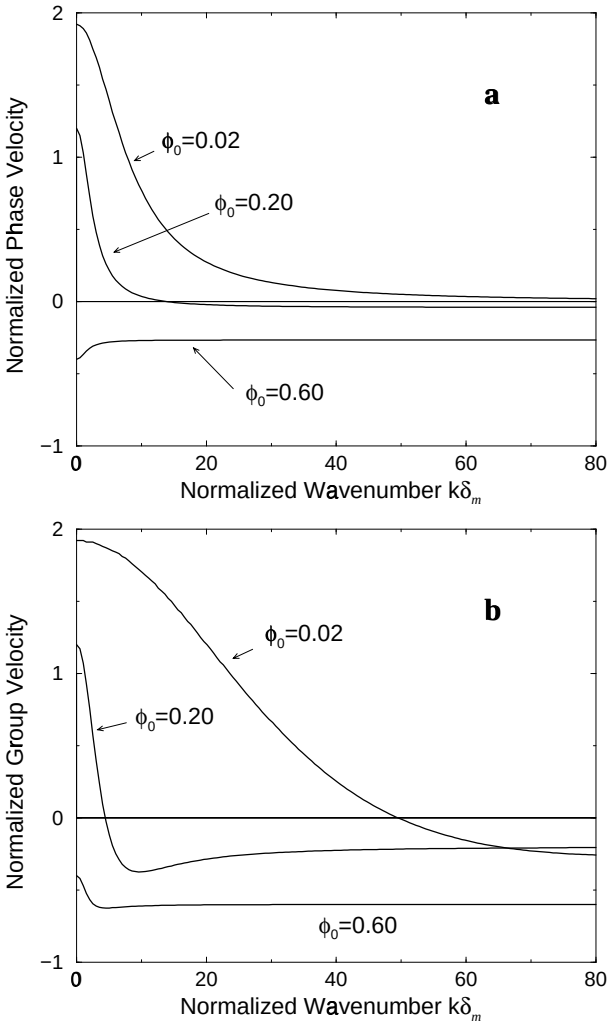

Figure 8. (a) Phase and (b) group velocities of vertically propagating porosity waves. The velocities are normalized by the melt extraction velocity (68). Three porosities are used 0.02, 0.20, and 0.60. We assume $\delta_f = 0$ and $K_0 = 1$. Small wave number (long wavelength) perturbations travel the fastest.

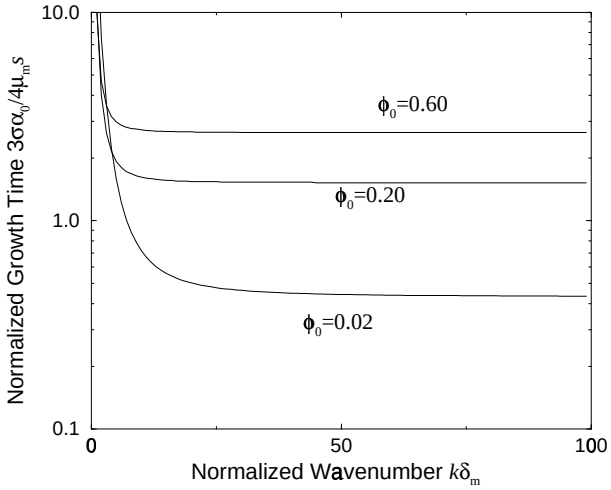

Figure 9. Normalized growth time of surface tension instabilities as a function of their normalized wave number for $a = b = 1/2$ in $G(\phi_0)$, $K_0 = 1$, $\delta_f = 0$, and $\phi_0 = 0.02, 0.20$ and 0.60, as in Figure 8. All wave numbers are unstable, but shorter-wavelength instabilities grow faster. Because the surface energy tends to $+\infty$ when the porosity vanishes, instabilities grow the fastest at small porosity.

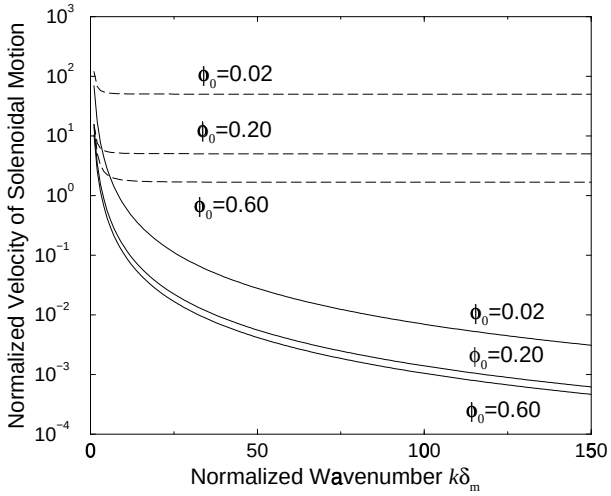

Figure 10. Matrix (solid lines) and fluid (dashed lines) vertical velocities of the solenoidal motions. The velocities are normalized by $\phi_0(1-\phi_0)\tilde{\phi}\Delta\rho/c$, i.e., the product of the melt extraction velocities by the amplitude of the porosity perturbation. We assume $\delta_f = 0$ and $\mathbf{k}\cdot\hat{\mathbf{z}} = 0$ and $\tilde{\phi} = 1$. At short wavelength (large wave number) only the fluid is in motion. At long wavelength (short wave number), fluid and matrix velocities become equal.

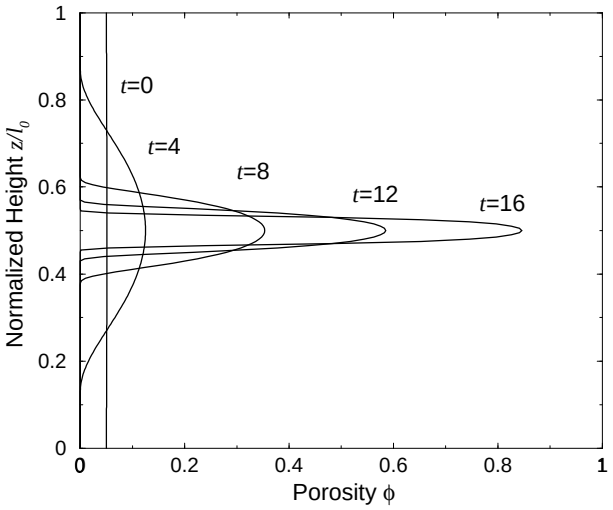

Figure 11. Porosity as a function of depth at different times for $\xi = 1$, $\lambda = 0$, and $\Delta\rho/\rho_m = 0$. The initial porosity has an average value of 0.05 and has a sinusoidal perturbation of wavelength l_0 and amplitude 0.001 with its maximum at $l_0/2$. The surface tension generates the instability. The Darcy term has been neglected. A single instability is produced.

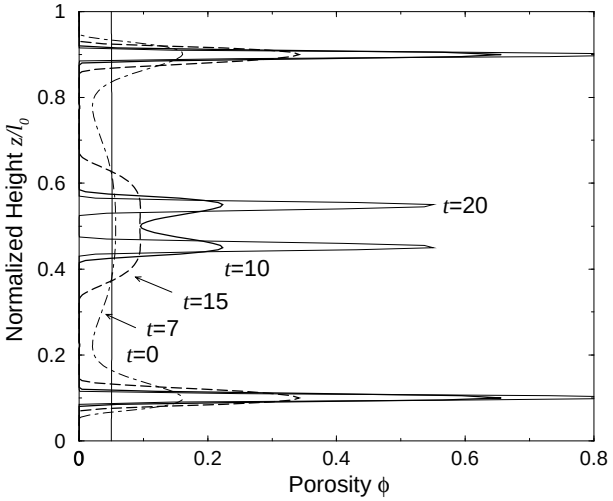

Figure 12. Porosity as a function of depth at different times for $\xi = 1$, $\lambda = 4$, and $\Delta\rho/\rho_m = 0$. The parameters are similar to those of Figure 11, but the Darcy term has been kept. Because of the presence of a Darcy resistance which prohibits the fluid from being drawn across large distances, the number of instabilities increases when compared to Figure 11.

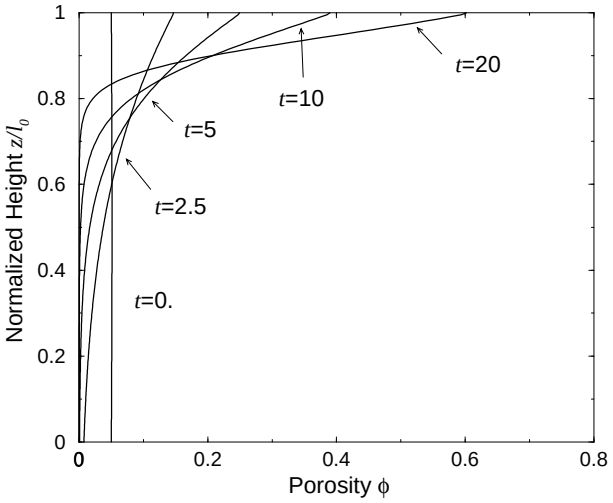

Figure 13. Porosity as a function of depth at different times for $\xi = 0$, $\lambda = 0$ and $\Delta\rho/\rho_m = 1$. The mixture is gravitationally unstable, and there is no surface tension. The matrix viscous term is dominant in the dynamics.

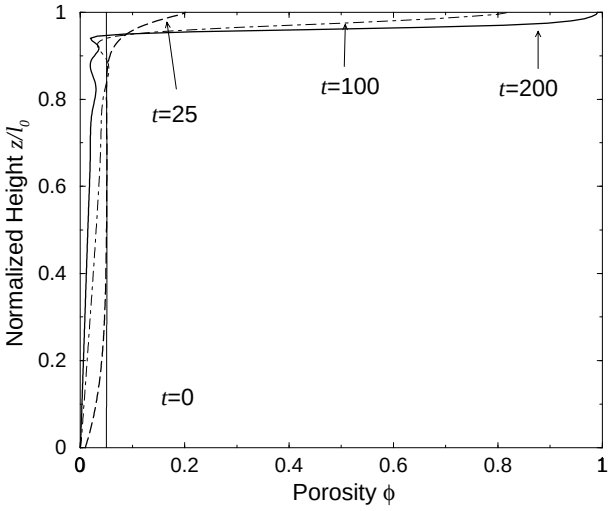

Figure 14. Porosity as a function of depth at different times for $\xi = 0$, $\lambda = 10$, and $\Delta\rho/\rho_m = 1$. The initial porosity is constant. The mixture is gravitationally unstable and without surface tension. Because of the presence of the Darcy term, porosity packets are generated.

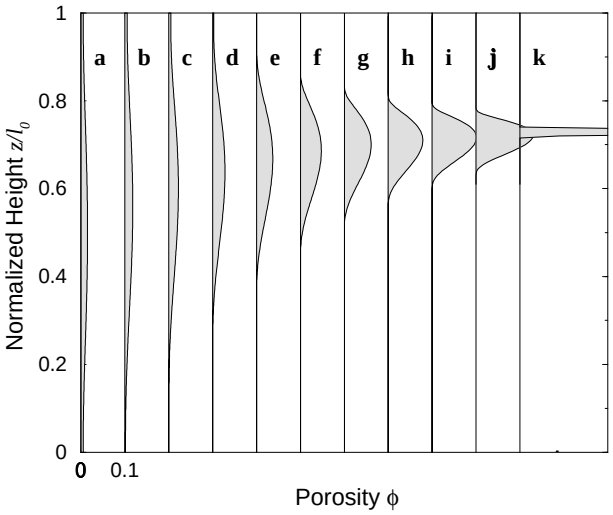

Figure 15. Time evolution (from (a) 0 years, (b) 120 kyr, (c) 250 kyr, (d) 420 kyr, (e) 620 kyr, (f) 850 kyr, (g) 1.1 Myr, (h) 1.4 Myr, (i) 1.8 Myr, (j) 2.2 Myr, to (k) 16 Myr) of porosity as a function of depth ($K_0 = 1$, $\Delta\rho = 500$ kg m^{-3}, $l_0 = 50$ m, $\delta_m = 8000$ m, $\mu_m = 10^{18}$ Pa s, $\rho_m = 3000$ kg m^{-3}, $\sigma\alpha_0 = 50$ kJ m^{-3}). For clarity,each profile as been x hifted by 0.1 porosity unit with respect to the previous profile. The initial porosity is a sinusoidal function with a maximum at $z/l_0 = 0.5$. The porosity wave travels upward until the surface tension dries the matrix at one point (at $t =$ 140 kyr, i.e., between Figures 15b and 15c). The evolution ultimately generates a sill of pure fluid (Figure 15k).

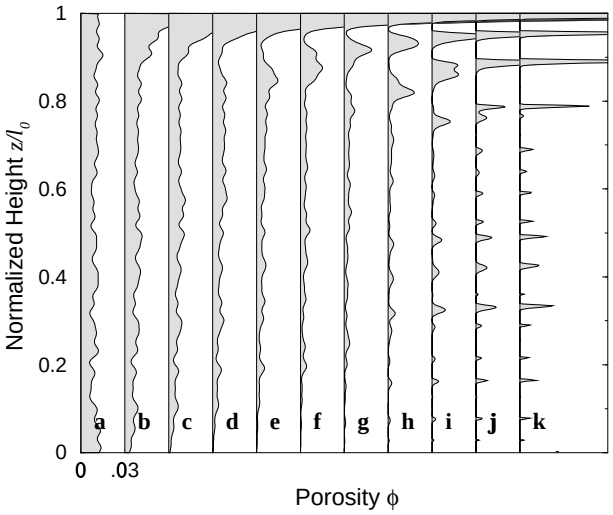

Figure 16. Same as Figure 15 but for a more complex initial porosity over a larger height ($K_0 = 1$, $\Delta\rho = 500$ kg m^{-3}, $l_0 = \delta_m = 8000$ m, $\mu_m = 10^{18}$ Pa s, $\rho_m = 3000$ kg m^{-3}, $\sigma\alpha_0 = 50$ kJ m^{-3}). Although long-wavelength harmonics are present in the starting porosity, the surface tension preferentially selects short wavelengths. The profiles are depicted at times (a) 0,(b) 15, (c) 29, (d) 47, (e) 70, (f) 100, (g) 140, (h) 240, (i) 400, (j) 600 and (k) 900 kyr.